

**Revealing the role of interfacial heterogeneous nucleation in metastable thin film
growth of rare-earth nickelates electronic transition materials**

Fengbo Yan^{1†}, Zhishan Mi^{1,2†}, Jinhao Chen¹, Haiyang Hu¹, Lei Gao^{1,3}, Jiaou Wang^{4*}, Nuofu*

Chen⁵, Yong Jiang¹, Lijie Qiao^{1,3} and Jikun Chen^{1}*

¹Beijing Advanced Innovation Center for Materials Genome Engineering, School of Materials Science and Engineering, University of Science and Technology Beijing, Beijing 100083, China

²China Iron & Steel Research Institute Group, Material Digital R&D Center, Beijing 100081, China

³Corrosion and Protection Center, University of Science and Technology Beijing, Beijing 100083, China

⁴Beijing Synchrotron Radiation Facility, Institute of High Energy Physics, Chinese Academy of Sciences, Beijing 100049, China

⁵School of Renewable Energy, North China Electric Power University, Beijing 102206, China

Correspondence: Prof. Lei Gao (gaolei@ustb.edu.cn), Prof. Jiaou Wang (wangjo@ihep.ac.cn), and Prof. Jikun Chen (jikunchen@ustb.edu.cn).

[†]Fengbo Yan and Zhishan Mi contributed equally to this work.

Abstract:

Although rare-earth nickelates ($ReNiO_3$, $Re \neq La$) exhibit abundant electronic phases and widely adjustable metal to insulator electronic transition properties, their practical electronic applications are largely impeded by their intrinsic meta-stability. Apart from elevating oxygen reaction pressures, heterogeneous nucleation is expected as an alternative strategy that enables the crystallization of $ReNiO_3$ at low meta-stability. In this work, the respective roles of high oxygen pressure and heterogeneous interface in triggering $ReNiO_3$ thin films growth at metastable state are revealed. The $ReNiO_3$ ($Re = Nd, Sm, Eu, Gd, \text{ and } Dy$) heterogeneous thin films growth on $LaAlO_3$ single crystal substrate have an effective crystallization at atmosphere without the necessity to apply high oxygen pressures, suggesting the interfacial bonding between the $ReNiO_3$ and substrates can sufficiently reduce the positive Gibbs formation energy of $ReNiO_3$, which is further verified by the first-principles calculations. Nevertheless, the abrupt electronic transitions only appear in $ReNiO_3$ thin films grown at high oxygen pressures, in which cases the oxygen vacancies are effectively eliminated via high oxygen pressure reactions as indicated by near-edge X-ray absorption fine structure (NEXAFS). This work unveils the synergistic effects of heterogeneous nucleation and high oxygen pressure on the growth of high quality $ReNiO_3$ thin films.

Keywords: Correlated oxides; Nickelates; Thin films; Metastable materials; Metal to insulator transitions

1. Introduction

The d -orbital correlation within transitional metal oxides enriches distinguished transportation functionalities such as metal to insulator transition (MIT) beyond conventional materials. One of the most important material family among the electronic transition oxide semiconductors is the rare-earth nickelates ($ReNiO_3$), the electronic orbital configuration of which experiences an abrupt and reversible transition from $Ni^{3+\Delta}$ to Ni^{3+} via elevating temperature across a critical point (T_{MIT}). As a result, the energy band gap of $ReNiO_3$ merges abruptly with the electronic conductivity transforming from insulator (or semiconductor) to metal. One distinguished advantage of $ReNiO_3$ family is the adjustable T_{MIT} with a broad range of 100 K-600 K by simply regulating their rare-earth composition^{1,2}. Apart from critical temperature, the MIT behavior of $ReNiO_3$ can be also triggered by stimuli such as polarized electric fields³⁻⁵, mechanical or interfacial strains⁶⁻⁸, and hydrogenation⁹⁻¹⁴. It is especially worthy to note that upon hydrogenation, the electronic structure of $ReNiO_3$ can be further reversibly triggered into the electron localized Ni^{2+} configuration, and the hydrogenated $ReNiO_3$ is electron insulating but proton conducting. Owing to their extreme complexity in the electronic phase diagram and multiple electronic orbital transitions, the $ReNiO_3$ is demonstrated to be useful in correlated electronic devices such as mutant and NTCR thermistor¹⁵, ocean electric field sensor¹³, photocatalysis¹⁶, correlated fuel cell¹², non-volatile logical devices⁴, and correlated bio-sensor¹⁷.

However, the above abundant applications in correlated electronics are largely bottlenecked by the intrinsic high metastability of $ReNiO_3$ ($Re \neq La$). In contrast to conventional oxide semiconductors, $ReNiO_3$ ($Re \neq La$) usually exhibits a positive formation free energy (ΔG)^{1,18} and cannot be synthesized by conventional solid-state reactions. Previous reports indicated that the synthesis of metastable $ReNiO_3$ ($Re \neq La$) relies on special conditions such as high oxygen pressure annealing^{19,20} and the template effect^{6,8,21} from the substrate. For example, Ramanathan *et al.*¹⁸ reported the non-epitaxial thin film growth of $SmNiO_3$ on silicon substrate via magnetron sputtering followed by high oxygen pressure annealing. They found that the non-epitaxial thin film growth of $SmNiO_3$ can be deposited successfully at the condition that ΔG is negative when the oxygen pressure and temperature are specific. Alternatively, the thin films of $ReNiO_3$ can be also epitaxially deposited on single crystalline perovskite substrates (e.g., $LaAlO_3$, $SrTiO_3$) by pulsed laser deposition (PLD)²² and metal organic chemical vapor deposition (MOCVD)²³ without oxygen post annealing. Since the required oxygen pressure in PLD or MOCVD is far below the atmosphere, it unveils the importance of heterogeneous nucleation in the synthesis of rare-earth nickelates. Although $ReNiO_3$ films can be deposited by the two mentioned methods, vacuum combined with heterogeneous nucleation is merely used to grow the low and medium metastability $ReNiO_3$ films such as $PrNiO_3$, $NdNiO_3$, $SmNiO_3$, $EuNiO_3$ and $GdNiO_3$ and rarely reported to synthesize high metastability $ReNiO_3$ films (e. g. $DyNiO_3$ and $ErNiO_3$). In addition, the synergistic application of heterogeneous nucleation and high oxygen pressure annealing in spin coating-assisted epitaxy growth is more likely to achieve deposition of medium and high metastability

$ReNiO_3$ films. Thus, it is still unclear that how the two growth conditions influence the thermodynamics of the growth of metastable $ReNiO_3$ film.

In this work, we unveil that the importance of interfacial heterogeneous nucleation via epitaxy to the material growth of metastable $ReNiO_3$. ($Re=Sm, Nd, Eu, Gd$ and Dy). The respective mechanisms to form a distorted perovskite structure of $ReNiO_3$, as associated to the interfacial heterogeneous nucleation or the high oxygen pressure related solid state reactions, were separately investigated. The lattice constant and electronic transportation properties are systematically investigated for $ReNiO_3$ epitaxy on $LaAlO_3$ (001) and $SrTiO_3$ (001) substrates at various oxygen pressures from 1atm to 15 MPa and covering various meta-stabilities of $ReNiO_3$. Assisted by the near-edge X-ray absorption fine structure analysis (NEXAFS), the variation in electronic orbital structures associated to Ni-L edge and O-K edge were compared for $ReNiO_3$ grown at 1 atm and 15 MPa oxygen pressures. Apart from experimental investigations, density functional theory (DFT) calculations were performed to reveal the driving force of heterogeneous nucleation ascribed to chemical interface interaction between $ReNiO_3$ films and substrates. To clarify the dominant role to the formation of $ReNiO_3$, the reductions in free energy associated to the interfacial heterogeneous nucleation via epitaxy were calculated and further compared to the one associated to the elevation in oxygen pressure.

2. Methods

DFT calculations: The DFT calculations were performed in the Vienna ab initio Simulation Package (VASP) ²⁴. The core electrons were described using the projector-augmented-wave (PAW) method and the electron exchange and correlation were modeled in GGA framework with the Perdew-Burke-Ernzerhof (PBE) form ^{25, 26}. All the calculations were carried out as spin-polarized. The plane-wave cutoff energy was set to 400 eV. During the geometrical optimizations, atoms were allowed to be relaxed until the forces on all the relaxed atoms were less than 0.01 eV/Å.

Sample preparation: The $ReNiO_3$ ($Re = Sm, Nd, Eu, Gd$ and Dy) thin films were grown via the wet chemical method using spin coating. $Re(NiO_3)_3 \cdot 6H_2O$ and $Ni(OCOCH_3)_2 \cdot 4H_2O$ were dissolved in ethylene glycol monomethyl ether according to the molar stoichiometric ration 1:1 and stirred for 2h using the magnetic stirrer. The obtained chemical solution was deposited on the $LaAlO_3$ (LAO) (001) and $SrTiO_3$ (STO) (001) substrates respectively by spin coating and then the substrates were dried at 175°C for 90s. Subsequently, the as-deposited thin films were annealed in a tubular furnace (OTF-1200X-HP-30) at 800°C for 3h with the heating rate 10°C/min to form single crystal $ReNiO_3$ thin films under different oxygen pressure.

Characterizations: These samples were characterized by X-ray diffraction (XRD) for phase identifications and analysis of variation of lattice constants. The resistivity of thin films was measured in vacuum within the temperature range from 300K to 500K using a commercialized CTA-system and from 5K to 300K using physical property measurement system (PPMS, Quantum Design Inc.), respectively. In order to reflect the valence variations in electronic structures of $ReNiO_3$, near-edge X-ray absorption fine structure (NEXAFS) was performed at BSRF-4b9b beam line of

Beijing Synchrotron Radiation Facility, Institute of High Energy Physics, Chinese Academy of Sciences.

3. Results and discussion

3.1. Role of interfacial nucleation via epitaxy on the lattice template of the substrate

The $ReNiO_3$ usually exhibits positive Gibbs free energy (ΔG) under the conventional growth conditions^{1, 18}, and therefore the $ReNiO_3$ cannot be synthesized using conventional solid-state reactions. Nevertheless, the $ReNiO_3$ thin films such as $SmNiO_3$, $NdNiO_3$ and $PrNiO_3$, can be indeed epitaxially grown on single crystalline perovskite substrates utilizing the template effects of the substrate lattice that triggers heterogeneous nucleation^{8, 27, 28}. In order to investigate the nucleation and growth mechanism of $ReNiO_3$ films associated to such heterogeneous process, a series of experimental conditions were used to grow $ReNiO_3$ films, including $SmNiO_3$ (SNO), $NdNiO_3$ (NNO), $EuNiO_3$ (ENO) and $GdNiO_3$ (GNO) on perovskite substrates via spin coating followed by high oxygen pressure annealing under various pressure.

In our experiment, $ReNiO_3$ ($Re = Sm, Nd, Eu$ and Gd) films were grown on LAO (001) and STO (001) substrates by the wet chemical method using spin coating then annealed at 800 °C under 1 atm and 15MPa oxygen pressure. It is noteworthy that $ReNiO_3$ films with medium and high metastability (e. g. $EuNiO_3$) cannot be synthesized on STO (001) substrates successfully²³, as is indicated by no resistance for these $ReNiO_3$ films. Previous works have reported that there exists a large lattice mismatch between $ReNiO_3$ and STO substrates in particular with Re element after Eu ²⁹, leading to the formation of relaxed array of nanocrystalline islands in the $ReNiO_3$ films²², which has also been observed in other perovskite oxide films such as $PbTiO_3/SrTiO_3$ ³⁰. Therefore, it is prone to form misfit dislocations or structure defects throughout the film especially in the low oxygen pressure, for example, $BaTiO_3/SrTiO_3$ ³¹. Since the films cannot be integrated together, the sample resistances are usually beyond the range of multimeter. In addition, it was also affirmed by reciprocal space mapping that the interfacial strain between $ReNiO_3$ films and STO substrate was relaxed⁷. From these aspects, the experimental results from various $ReNiO_3$ thin films deposited on LAO substrates are more reliable and convincing compared to those from $ReNiO_3$ thin films on STO substrates.

To characterize structure quality of samples grown via heterogeneous nucleation followed by oxygen annealing process, X-ray diffraction (XRD) was performed and the results are demonstrated in Fig.1. Fig. 1a-c shows the X-ray θ - 2θ scans taken on $ReNiO_3$ ($Re = Sm, Nd$ and Eu) films grown on LAO (001) substrates under the oxygen annealing pressure of 1atm and 15 MPa at 800°C. The diffraction peaks of SNO, NNO and ENO thin films locate beside the diffraction peaks of LAO substrates, indicating the single crystalline of these thin films grown on LAO (001) substrates at both oxygen annealing pressure of 1 atm and 15 MPa (see XRD patterns at a broader scanning range in Fig. S1. While some additional diffraction peaks can be seen in these XRD patterns, the intensity of these additional diffraction peaks is much lower

than that of the (00 l) peaks associated with $ReNiO_3$ thin films such as (001), (002) and (003). The advantageous interfacial strain between as-grown $ReNiO_3$ thin films and the LAO substrates has been reported in our previous reports^{7,32,33}. Since the $ReNiO_3$ films can be grown on LAO substrates even under low oxygen pressure, the heterogeneous nucleation rather than oxygen pressure plays an important role in stabilizing the distorted perovskite structure of as-grown $ReNiO_3$ in metastable manner. In the past, it was generally accepted that strain energy between $ReNiO_3$ thin film and substrate plays a crucial role in the nucleation stage of rare earth nickelate phase because $ReNiO_3$ phase is only deposited on perovskite substrates such as $LaAlO_3$ and $SrTiO_3$ while only the mixture of rare-earth oxide and NiO phase is grown on other type substrates such as MgO , YSZ³⁴ and $ZrO_2(Y_2O_3)$ ²³. Besides, the magnitude of the strain also has an important influence on the formation of $ReNiO_3$ phase. The smaller lattice strains of $ReNiO_3$ thin films on LAO than STO substrates shown in Table 1 confirm the growth of $ReNiO_3$ films on LAO is favorable. For example, $GdNiO_3$ single phase is only successfully deposited on LAO substrate owing to lower lattice mismatch^{23,35}. However, the thickness of samples prepared in our experiment is about 10nm and therefore the strain energies between $ReNiO_3$ thin films and LAO substrates are expected to be not quite large when the volume of nucleus is small enough. In this case, strain energy will be not sufficient to overcome the nucleation barrier, instead interfacial chemical energy will become a key role to decide whether heterogeneous nucleation is formed. In order to verify this point, the DFT calculations of the interface free energies of samples were performed, as is shown in Fig. 2. Fig. 2a-b illustrate the crystal structures of $ReNiO_3$ and substrates for LAO and STO, respectively. Fig. 2c shows $SmNiO_3/LaAlO_3$ and $SmNiO_3/SrTiO_3$ interface structures adopted in DFT calculations. Fig. 2d shows the interface free energies of as-grown $ReNiO_3$ films on LAO and STO substrates, where the specific interface free energy is defined as:

$$E_i = (E_{interface} - E_{up} - E_{down})/S \quad (1)$$

where $E_{interface}$ is the total interface free energy of the interface structure. E_{up} is the energy of the upper $ReNiO_3$ film. E_{down} is the energy of the lower substrate and S is the area of interface. All the calculated interface free energies are negative and therefore the interface free energy is expected to descend the pristine positive free energy of $ReNiO_3$ to trigger heterogeneous nucleation of $ReNiO_3$ films on LAO and STO substrates. In addition, the more negative interface free energies when epitaxy $ReNiO_3$ thin films grown on LAO compared to STO indicate the interfaces of $ReNiO_3$ films on LAO are more stable. The interfacial charge transfer of the interface structure can further describe the interfacial bonding strength between $ReNiO_3$ films and LAO and STO substrates, and the calculated results are shown in Fig. 2e-f. The differential charge density at the interface along the c-axis direction is defined as

$$\Delta\rho = \rho_{interface} - \rho_{up} - \rho_{down} \quad (2)$$

where $\rho_{interface\ structure}$ represents the total charge density of the system, ρ_{up} and ρ_{down} represent the charge density of upper film structure and lower substrate structure. A positive value of $\Delta\rho$ represents valence electron increasing and a negative value of $\Delta\rho$ represents electron decreasing. The $ReNiO_3$ films grown on

LaAlO₃ have larger charge transfer magnitudes comparing with those on SrTiO₃ (as shown in Fig. S2, indicating stronger interface bonding strength and larger film growth driven force. Thus, smaller interface lattice strain and the more negative interface free interfaces are the dominant factors to facilitate the heterogeneous nucleation of *Re*NiO₃.

Table 1

Lattice strain of the a-axis and b-axis (More details are shown in section 2 of supplementary material). The results indicate the oxides grown on LaAlO₃ have smaller lattice strain.

	LaAlO ₃		SrTiO ₃	
	a	b	a	b
SmNiO₃	-0.021	0.008	-0.056	-0.028
NdNiO₃	-0.014	0.013	-0.049	-0.024
EuNiO₃	-0.011	-0.009	-0.047	-0.045
GdNiO₃	-0.029	0.021	-0.064	-0.016

3.2. Role of the elevation in oxygen pressure

Apart from heterogeneous nucleation, oxygen pressure was also expected as another key point to influence the growth of *Re*NiO₃ films³⁶. To further investigate the properties of metastable *Re*NiO₃ associated to different oxygen pressures, the electrical transportation properties of *Re*NiO₃ films under two selected oxygen pressure conditions are investigated. The measured temperature-dependent in-plane electrical resistivity for *Re*NiO₃ thin films with various rare-earth elements (*Re* = Sm, Nd, Eu and Gd) on LAO and STO substrates at 1atm and 15 MPa oxygen pressure is shown in Fig. 3. The MIT behaviors of the as-deposited SNO/LAO and SNO/STO under 1atm measured via both heating up and cooling down processes are shown in Fig. 3a. It is worth noting that for SNO/LAO and SNO/STO under 1atm, the obtained MIT behavior is very flatten compared with those as-deposited at 15 MPa oxide pressure, indicating the MIT behavior is suppressed for the *Re*NiO₃ film grown under 1 atm. As for the ρ -*T* curves, it can be observed that the SNO/LAO system heating up and cooling down profiles are sharper than those of SNO/STO system, which is attributed to large interface strain of the SNO/STO system⁷. Meanwhile, as shown in Fig. 3b, the ρ_T/ρ_{300K} decreases more remarkably for the SNO/LAO system than that of SNO/STO system at 15 MPa oxygen pressure, which is consistent with the results in Fig. 3 a. In Fig. 3c-d, the MIT behaviors for NNO, ENO and GNO on LAO under 1atm and 15 MPa oxygen pressure are similar compared to SNO. However, it is also noteworthy that an obvious hysteresis in T_{MIT} can be seen for NNO on LAO and STO as shown in Fig. 3c when measuring the *R*-*T* curve via heating up compared to cooling down, which has also been reported by the previous literatures^{7, 37, 38} that the ρ -*T* curves measured through heating up and cooling down exist a hysteresis for *Re*NiO₃ with larger rare-earth elements taking up the A-site of the perovskite structure.

Therefore, it can be found that without the high oxygen pressures, the MIT behaviors of $ReNiO_3$ films on LAO and STO substrates under 1 atm behave poorly, which might be caused by oxygen vacancies since $ReNiO_3$ are prone to form oxygen vacancies under low oxygen pressure^{36, 39}. It has been reported that the presence of oxygen vacancies can alter the Ni valence state from Ni^{3+} to Ni^{2+} via offering electrons from the missing oxygen atoms^{36, 40-42}. Moreover, owing to radius of Ni^{3+} ($r=0.56\text{\AA}$) being smaller than that of Ni^{2+} ($r=0.69\text{\AA}$), oxygen vacancies enlarge out-of-plane lattice parameter, which is verified by Fig. 1d. As for in-plane lattice, owing to the good lattice match between LAO and $ReNiO_3$, the in-plane lattice is independent of the oxygen pressure and coincide with that of LAO. In this case, it can be further inferred that the expansion of the lattice constants of $ReNiO_3$ expand Ni-O bonds and changes the rotations and tilts of NiO_6 octahedra⁴³. Further, the larger Ni-O bonds can also induce the smaller Ni-O-Ni bond angle owing to the reduce of tolerance factor, which decreases the bandwidths. Moreover, the reduced bandwidths make the Coulomb repulsion between the electrons stronger, as a result, leading to the suppression of MIT behaviors of $ReNiO_3$ films grown under low oxygen pressure. More importantly, the high oxygen pressure provides sufficient oxygen atoms for the growth of $ReNiO_3$ films on substrates to ensure elements in $ReNiO_3$ satisfying the specific stoichiometric ratio.

In order to verify the oxygen vacancies indeed alter the valence state of Ni from +3 to +2 under low oxygen pressure, the near edge X-ray absorption fine structure (NEXAF) analyses have been performed and the results are shown in Fig. 4. Comparing the O: K-edge EXAFS spectra of $SmNiO_3$ and $NdNiO_3$ at 1atm with those at 15MPa oxygen pressure in Fig. 4a and 4c respectively, we can distinctly observe the increased pre-peak (the first peak in the low photon energy) in the spectra for SNO/LAO and NNO/LAO under the higher oxygen pressure. The O-K edge pre-peak is related to the strong covalency between the Ni 3d and O 2p states. Therefore, the low O-K edge pre-peak intensity suggests the large amount of oxygen vacancies which alter the Ni^{3+} to Ni^{2+} . In this case, to some degree, the pre-peak in their O: K-edge spectra reflects the relative content of Ni^{3+} or Ni^{2+} ⁷, which means the higher content of Ni^{3+} owing to the higher O-K edge pre-peak intensity when the annealing oxygen pressure is 15MPa for both SNO/LAO and NNO/LAO. With respect to the Ni: L_3 spectra, the split peaks in Fig. 4b and 4d originate from the transition from Ni-2p to Ni-3d, which suggests the proportion of the Ni^{3+} compared to the Ni^{2+} is represented by the relative height of peak in high photon energy to the peak in low photon energy for SNO/LAO and NNO/LAO, respectively. Therefore, the as-grown SNO thin film and NNO thin film on LAO substrates under 15MPa contain more Ni^{3+} , further confirming that oxygen vacancies change the valence state of Ni from +3 to +2. In addition, it can also be seen that under the same synthesis condition, the relative content of Ni^{3+} in NNO/LAO is higher than that in SNO/LAO from the Ni: L_3 edge and O: K edge spectra respectively which is consistent with the previous reports^{7, 44, 45}.

Meanwhile, to explicate the role of oxygen vacancies on the transport properties of $ReNiO_3$ in the insulator region, the low temperature electrical transportation of the $ReNiO_3/LaAlO_3$ (001) were characterized and analyzed. The evolutions of ρ_T/ρ_{300K} versus temperature about $ReNiO_3/LaAlO_3$ systems are illustrated in Fig. 5a, which suggests the profiles of SNO, ENO and GNO under 15MPa are steeper compared to those under the low oxygen pressure. According to references ⁴⁶⁻⁴⁹, the $ReNiO_3$ generally exhibits a Mott variable range hopping (VRH) mechanism in the insulator region, which can be confirmed by the linearity of $\ln(\rho_T/\rho_{300K})-T^{-0.25}$. VRH model describes the transportation mechanism of carriers in the low temperature range that a carrier hops to the site with a closer energy rather than the nearest position ⁵⁰. It can be described by means of the following expression

$$\rho(T) = \rho_0 \exp\left(\frac{T_0}{T}\right)^p \quad (3)$$

where ρ_0 is the prefactor, T_0 is the characteristic temperature, p is the exponent related to the conduction mechanism. In three dimensions, $p=1/4$ and T_0 can be determined by

$$T_0 \equiv T_{Mott} = \frac{18}{k_B N(E_F) a^3} \quad (4)$$

where $N(E_F)$ is the density of states (DOS) close to Fermi energy (E_F) and a is the localization length of carriers. More details of the fitting results of $\ln(\rho_T)-T^{-0.25}$ are given in Fig. S3 as discussing carrier transport model of $ReNiO_3$ in three dimensions.

In the meanwhile, the thickness of the $ReNiO_3$ grown by chemical depositions is approximately 10nm. Therefore, we also fitted the ρ_T-T tendencies via two dimensional carrier transport model that can be expressed as $\ln(\rho_T)-T^{-1/3}$, as shown in Fig. S4. The values of T_{Mott} obtained in three dimensions are illustrated in Fig. 5b, which are generally smaller in low oxygen pressure. According to the reference ⁵¹, T_{Mott} characterizes the degree of the disorder. Fig. 5b indicates the disorder of $ReNiO_3$ grown on LAO via chemical deposition increases with the oxygen pressure increasing, since the deficient oxygen atoms in low oxygen pressure are apt to form oxygen vacancies in the process of $ReNiO_3$ films growth, leading to the formation of Ni^{2+} and decrease of disorder. Thus, the oxygen pressure plays a critical role in controlling stoichiometric ratio of $ReNiO_3$. Meanwhile, it is worthy to be mentioned that the behavior of T_{Mott} of other $ReNiO_3$ is consistent with $SmNiO_3$. Nevertheless, it has been reported ⁵² that $ReNiO_3$ is a multiple-band system with both electron- and hole-like carriers and therefore the variation of carrier mobility under low temperature is very complicate, possibly leading to the appearance of some anomalous points, such as $EuNiO_3$ annealed under 4Mpa and $GdNiO_3$ annealed at 1atm. In Fig. 5c, the seebeck coefficient of $ReNiO_3$ thin films on LAO substrates at room temperature is plotted as a function of the oxygen pressure. The obtained results show the seebeck coefficients at room temperature of $ReNiO_3$ thin films such as $SmNiO_3$, $NdNiO_3$ and $EuNiO_3$ keep negative whether annealed in low or high oxygen pressure, while the seebeck coefficient of GNO changes from negative to positive when oxygen pressure increases from 1atm to 15MPa, suggesting the carrier type becomes p-type. Similar phenomenon has also been reported in reference ⁵³ and the reason is expected to be

oxygen vacancies.

According to above results, it can be concluded that high oxygen pressure is beneficial to maintaining the valence state of Ni^{3+} by eliminating oxygen vacancies and abrupt electronic transitions of ReNiO_3 films.

3.3 Metastable ReNiO_3 thin film growth combining epitaxy and high oxygen pressure

Since heterogeneous nucleation reduces the intrinsic positive Gibbs free energy and high oxygen pressure can eliminate oxygen vacancies to maintain the valence state of Ni^{3+} , the thin film growth of ReNiO_3 using chemical based spin coating process provides the opportunity to achieve thin film growth of ReNiO_3 with high metastability (e. g. Re from Dy to Tm) that has been rarely reported previously^{33,44}. As a representative case, the DyNiO_3 can be epitaxially grown on LaAlO_3 (001) single crystalline substrate via spin coating process of $\text{Dy}(\text{NiO}_3)_3 \cdot 6\text{H}_2\text{O}$, $\text{Ni}(\text{OCOCH}_3)_2 \cdot 4\text{H}_2\text{O}$ precursors dissolved in 2-methoxyethanol followed by annealing at 15MPa oxygen pressure at 800°C. Fig. 6a shows the R - T tendency of as-grown DNO/LAO, where a remarkable negative temperature coefficient resistance (NTCR) property is observed although the resistivity of DyNiO_3 thin film on LAO substrate deviates the normal values when temperature reaches to 525K that is not MIT temperature. The deviation could be attributed to high metal-to-insulator transition temperature destroys the integrity of interfacial structure between DNO thin films and LAO substrates. And the corresponding crystal structure illustration of DyNiO_3 is shown in Fig. 6c. Although the complete R - T curve reflecting the metal to insulator transition is not measured successfully in DyNiO_3 thin films, the temperature of metal to insulator transition has rarely been obtained via resistivity variation as a function of temperature for high metastability ReNiO_3 powders such as DyNiO_3 , HoNiO_3 in previous reports. For example, García-Muñoz *et al.*⁵⁴ provided R vs T curves for YNiO_3 ceramics up to 750K with a quite high oxygen pressure to synthesize. As a result, the determination of T_{MIT} for high metastability ReNiO_3 powders generally utilizes the DSC analysis⁵⁵ and neutron diffraction⁵⁶.

Another overwhelming advantage to grow ReNiO_3 thin films using chemical based precursors, compared to the previously reported vacuum-based approaches, is the capability to achieve more flexible and convenient adjustment in the rare-earth composition. The rare-earth composition within ReNiO_3 regulates the distortion in NiO_6 octahedron that determines the electronic structure and T_{MIT} , and to achieve the continuous regulation of T_{MIT} within a wide range of temperature, the effective growth of ReNiO_3 with multicomponent of Re is required. Besides, the growth of ReNiO_3 thin films with various Re elements can not only help us to know how to stabilize of such a multi Re system in a single crystalline to further explore electronic behavior and metal to insulator transition mechanism but also allow us to investigate the phase transition mechanism around the triple point of the ReNiO_3 phase diagram^{57,58}. Patel *et al.*⁵⁷ has grown nickelate films with 5 different cations in the A-site and excellent crystallinity using PLD, the variation of Re compositions in target preparation process is not convenient. Compared to the vacuum-based approaches

such as PLD or magnetron sputtering, the rare-earth composition of the chemical deposited $ReNiO_3$ can be flexibly and quantitatively regulated by the combination of $Re(NiO_3)_3 \cdot 6H_2O$ with various compositions of Re according to the required stoichiometric ratio. As a representative example, $Nd_{0.3}Sm_{0.4}Gd_{0.3}NiO_3$ thin film was grown on LAO substrates via spin coating method of $Nd(NiO_3)_3 \cdot 6H_2O$, $Sm(NiO_3)_3 \cdot 6H_2O$ and $Gd(NiO_3)_3 \cdot 6H_2O$ and $Ni(OCOCH_3)_2 \cdot 4H_2O$ precursors dissolved in 2-methoxyethanol according to the molar ratio 0.3:0.4:0.3:1 followed by annealing at 15MPa oxygen pressure at 800°C. Fig. 6b shows the resistivity variation as a function of temperature and the metal to insulator transition temperature is estimated around 373K. Meanwhile, the corresponding crystal structure illustration for $Nd_{0.3}Sm_{0.4}Gd_{0.3}NiO_3$ is shown in Fig. 6d.

3.4. Estimating the free energy reduction of interface chemical bonds from thermodynamic perspective

In previous researches, it was generally known that strain induced by the film-substrate mismatch is the most factor to influence the nucleation of $ReNiO_3$ phase²². However, it is worthy of note that strain energy may not work when both the nucleation volume and thickness of the thin film are very small³⁵, suggesting another factor is critical in the formation of $ReNiO_3$ phase. It is expected to be the interface free energy.

In order to explain the role of interface free energy, we estimated the interface free energy and Gibbs free energy of formation for $ReNiO_3$ as the following: the interface free energy was calculated by DFT modeling while the Gibbs free energy of formation for bulk $ReNiO_3$ were obtained when $ReNiO_3$ thin films were grown on substrates with no lattice mismatch such as oxidized silicon wafers. The DFT calculated results are listed in the Table 2. And the formation of bulk $ReNiO_3$ in our experiment can be expressed as the following:



where Re is the rare-earth element.

According to the reference¹⁸, the molar Gibbs free energy of formation for bulk $ReNiO_3$ via reaction (6) can be expressed as the following formula:

$$\Delta G = \Delta H_{LNO,1000K} - T\Delta S_{LNO,1000K} + (h - sT)(r(Re^{3+}) - r(La^{3+})) - (1/4)RT\ln(P/p) \quad (6)$$

LNO stands for $LaNiO_3$, R is the ideal gas constant, the P accounts for oxygen pressure with MPa unit, and p represents the standard atmospheric pressure (0.1MPa). According to references^{18,59}, the enthalpy and entropy changes for this reaction at 1000K are $\Delta H_{LNO,1000K} = -46.07 \text{kJmol}^{-1}$ and $\Delta S_{LNO,1000K} = -26.4 \times 10^{-3} \text{kJ(K}^{-1}\text{mol}^{-1})$. h and s obtained from reference¹⁸ represent the trend in enthalpy and entropy respectively. The values of them are $h = -356 \text{kJmol}^{-1}\text{\AA}^{-1}$, $s = -0.125 \text{kJK}^{-1}\text{mol}^{-1}\text{\AA}^{-1}$ (see more details in Section 5 of supplementary material). $r(Re^{3+})$ and $r(La^{3+})$ are the radii of Re^{3+} and La^{3+} , respectively. Here, we use $r(Sm^{3+}) = 1.24 \text{\AA}$, $r(Nd^{3+}) = 1.27 \text{\AA}$, $r(Eu^{3+}) = 1.20 \text{\AA}$ and $r(Gd^{3+}) = 1.19 \text{\AA}$, which have been reported in reference⁶⁰. Consequently, the

thermodynamic phase stability diagrams for SNO, NNO, ENO and GNO are shown in Fig. 7, along with points representing reported synthesis conditions for these materials.

As shown in Fig. 7, the ordinary synthesis conditions of the powder SNO and NNO are above the white region, which are indicated by solid cyan circle and solid orange diamond for SNO powder in Fig. 7a and solid cyan circle for NNO powder in Fig. 7b, respectively. However, the other points below the white region in Fig. 7 have been also confirmed to achieve the growth of $ReNiO_3$ films on $LaAlO_3$ substrates. It has been mentioned above that the main reason is heterogeneous nucleation stabilizing the distorted perovskite structure in metastable manner, whose driving force is practically from the interface free energies between $ReNiO_3$ films and substrates. To reveal this interface chemical effect, the ΔG calculated by eqn (7) for every condition to grow $ReNiO_3$ films on LAO substrates and the corresponding interfacial free energies calculated by DFT are listed and demonstrated in the Table 2.

To enable the comparison between the Gibbs free energy (ΔG) obtained from eqn (6) and interfacial chemical energy calculated by DFT, we assumed the following conditions: (1) the film thickness is 10nm, (2) a molar density is approximately 0.015mol cm^{-3} ¹⁸, (3) the interfacial free energy remains constant when the oxygen pressure varies. It is noteworthy in Table 2 that the Gibbs free energy of formation of bulk $ReNiO_3$ in reaction (5) is less than the interfacial chemical energy for SNO/LAO, NNO/LAO, ENO/LAO and GNO/LAO under the given conditions, which means the $ReNiO_3$ thin films ($Re=Sm, Nd, Eu$ and Gd) can be deposited on $LaAlO_3$ substrates and further affirms the interface free energy is efficient to reduce the Gibbs free energy. These discoveries give us a new insight into homogeneous nucleation and growth of $ReNiO_3$. For example, it is commonly recognized that heterogeneous nucleation caused by substrate template effect is not as important as high oxygen pressure to determine the nucleation of $ReNiO_3$ phase. However, the experimental and DFT calculation results in this study suggest in spin coating-assisted epitaxy growth, heterogeneous nucleation dependent on substrate template effect is the key factor to induce the nucleus of $ReNiO_3$ while the role of high oxygen pressure is essential to eliminate oxygen vacancies and maintain the valance of Ni^{3+} within $ReNiO_3$ to achieve an abrupt MIT performance.

Table 2

Gibbs free energy of formation of bulk $ReNiO_3$ according to eqn (6) for different synthesis conditions and the Interface free energy for $ReNiO_3/LAO$ (001)

samples	Condition	$\Delta G(\text{kJ/mol})$	$\Delta G(\text{eV}/\text{\AA}^2)$	Interface free energy($\text{eV}/\text{\AA}^2$)
SNO/LAO	1273K 7MPa	-0.0790	-7.4084e-04	-0.23072
	953K 10^{-3} MPa	16.6362	0.1560	
	953K 0.1MPa	7.5142	0.0704	
	1073K 15MPa	-2.2927	-0.0215	
NNO/LAO	953K 0.1MPa	0.4080	0.0038	-0.22188
	1123K 0.1MPa	2.9835	0.0280	

	1073K 15MPa	-8.9489	-0.0839	
ENO/LAO	1073K 15MPa	6.5823	0.0617	-0.23848
GNO/LAO	1073K 15MPa	8.8011	0.0825	-0.23025

4. Conclusions

In conclusion, the dominant roles of interfacial heterogeneous nucleation and high oxygen pressure related solid state reactions on the crystallization and growth of $ReNiO_3$ ($Re=Sm, Nd, Eu, Gd$ and Dy) covering various metastability are distinguished. From the one aspect, the interfacial template effect between $ReNiO_3$ and single crystalline perovskite oxide substrate triggers the heterogeneous nucleation and results in the nucleation of metastable $ReNiO_3$ without the necessity to apply high oxygen pressures. This understanding is well supported by the density functional theory (DFT) calculations, where the driving force of heterogeneous nucleation is ascribed to chemical interface interactions between films and substrates that sufficiently descend the positive formation energy of $ReNiO_3$. From the other aspect, although the metastable $ReNiO_3$ can be stabilized by epitaxy on $LaAlO_3$ substrate at normal pressure, their metal to insulator transition abruptness is largely reduced owing to the derivation of electronic structures from Ni^{3+} towards Ni^{2+} as indicated by near-edge X-ray absorption fine structure analysis. This highlights the necessity of the high oxygen pressure in compensating the oxygen vacancy within $ReNiO_3$ that maintains the abruptness of their temperature induced metal to insulator transitions. The synergistic effects of heterogeneous nucleation and high oxygen pressure guarantee the spin coating-assisted epitaxy growth of $ReNiO_3$ thin films with high intrinsic metastability.

Acknowledgments

This work was supported by the National Key Research and Development Program of China (No. 2018YFB0704300) and the National Natural Science Foundation of China (No. 62074014 and 52073090), the Fundamental Research Funds for the Central Universities (No. FRF-TP-19-023A3Z), and the Beijing New-star Plan of Science and Technology (No. Z191100001119071).

Competing interests

We declare no competing financial interest.

Additional information: Supplementary Information is available for this manuscript.

Correspondence: Prof. Lei Gao (gaolei@ustb.edu.cn), Prof. Jiaou Wang (wangjo@ihep.ac.cn), and Prof. Jikun Chen (jikunchen@ustb.edu.cn).

Figure and Caption

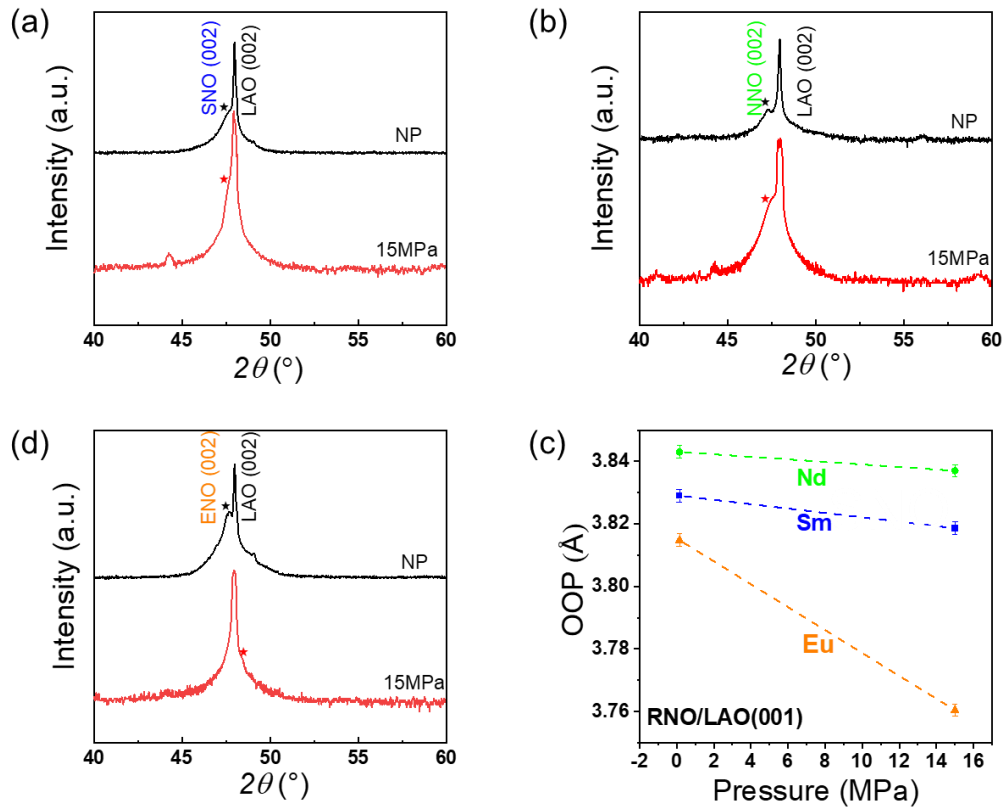


Fig. 1. X-ray diffraction patterns (θ - 2θ scans) of as-grown (a) SmNiO₃/LaAlO₃ (001) (b) NdNiO₃/LaAlO₃ (001) and (c) EuNiO₃/LaAlO₃ (001) under the annealing pressure of normal pressure and 15MPa with the same annealing temperature ($T=800^\circ\text{C}$). (d) Calculated results of out-of-plane lattice constants for as-deposited $Re\text{NiO}_3/\text{LaAlO}_3(001)$ ($Re=\text{Sm}, \text{Nd}, \text{Eu}$) thin films. The XRD data for SNO/LAO and ENO/LAO under 15MPa are from the reference⁶¹.

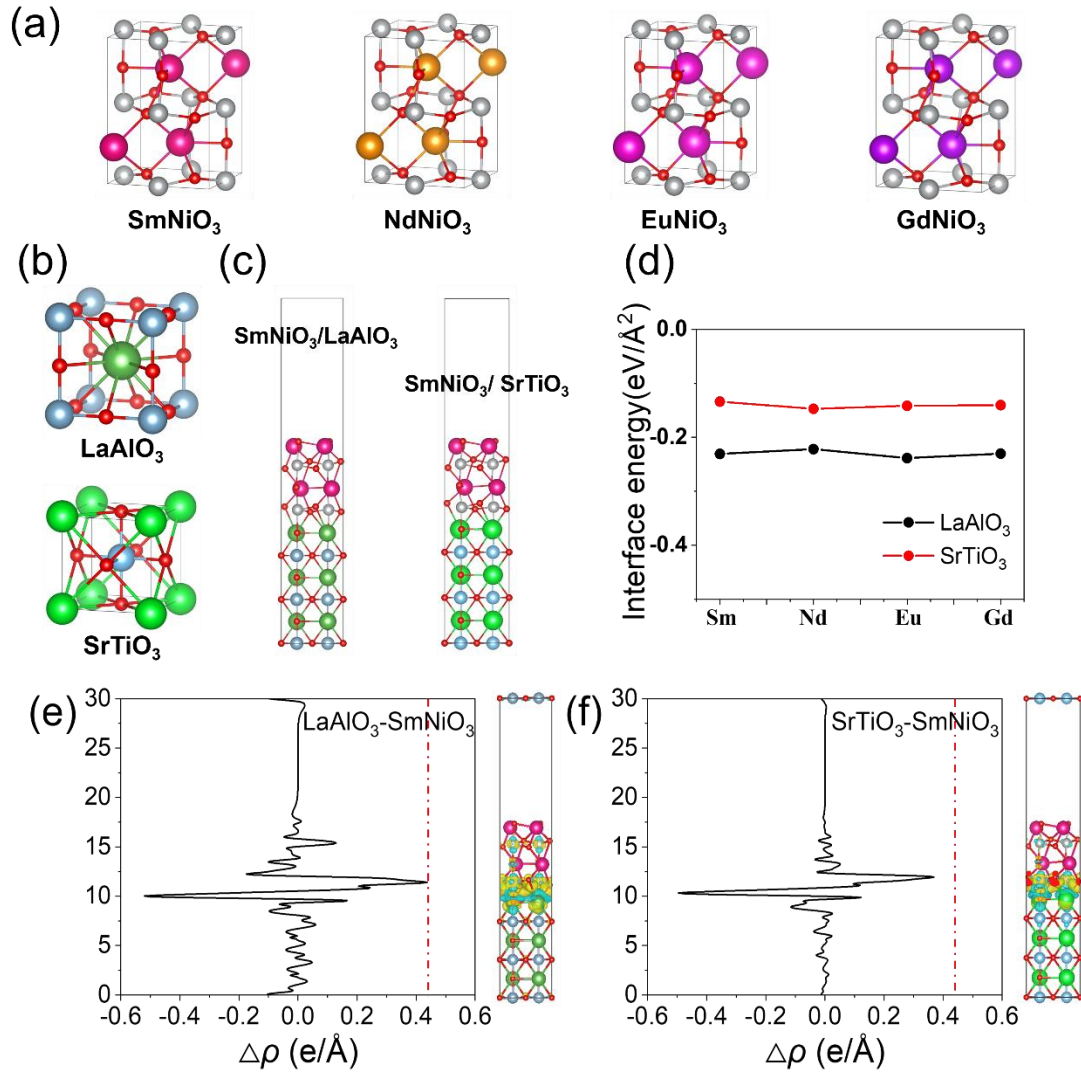


Fig. 2. (a) Unit cells of SmNiO₃, NdNiO₃, EuNiO₃, GdNiO₃. (b) Unit cells of LaAlO₃ and SrTiO₃. (c) SmNiO₃-LaAlO₃ interface and SmNiO₃-SrTiO₃ interface. (d) Interface energies of eight different interfaces. (e) the interfacial charge transfer of LaAlO₃-SmNiO₃ interface (f) SrTiO₃-SmNiO₃ interface.

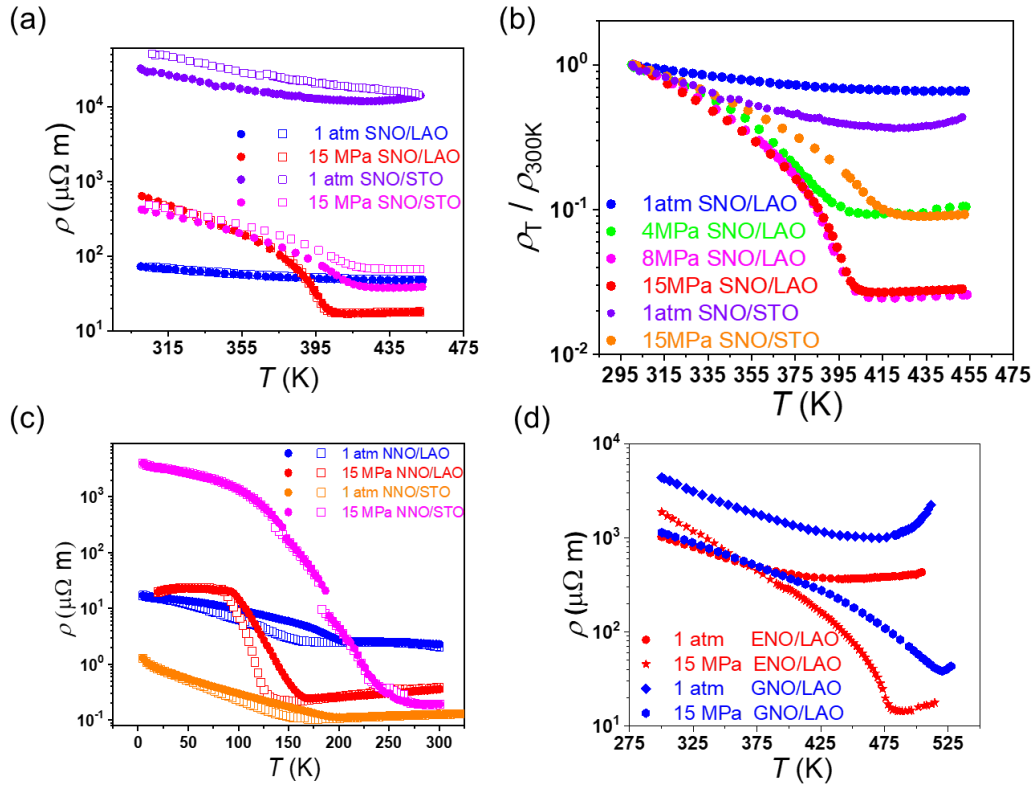


Fig. 3. (a) Temperature dependence of the resistivity for SmNiO₃/LaAlO₃ and SmNiO₃/SrTiO₃ under 1atm and 15MPa. (b) Temperature dependence of ρ_T/ρ_{300K} for SmNiO₃/LaAlO₃ under various annealing oxygen pressure and for SmNiO₃/SrTiO₃ under 15MPa. (c) Temperature dependence of the resistivity for NdNiO₃/LaAlO₃ under 1atm and 15MPa and for NdNiO₃/SrTiO₃ under 15MPa. (d) Temperature dependence of resistivity for EuNiO₃/LaAlO₃ and GdNiO₃/LaAlO₃ under 1 atm and 15MPa. The solid symbols represent the heating processes, while the hollow symbols represent the cooling processes.

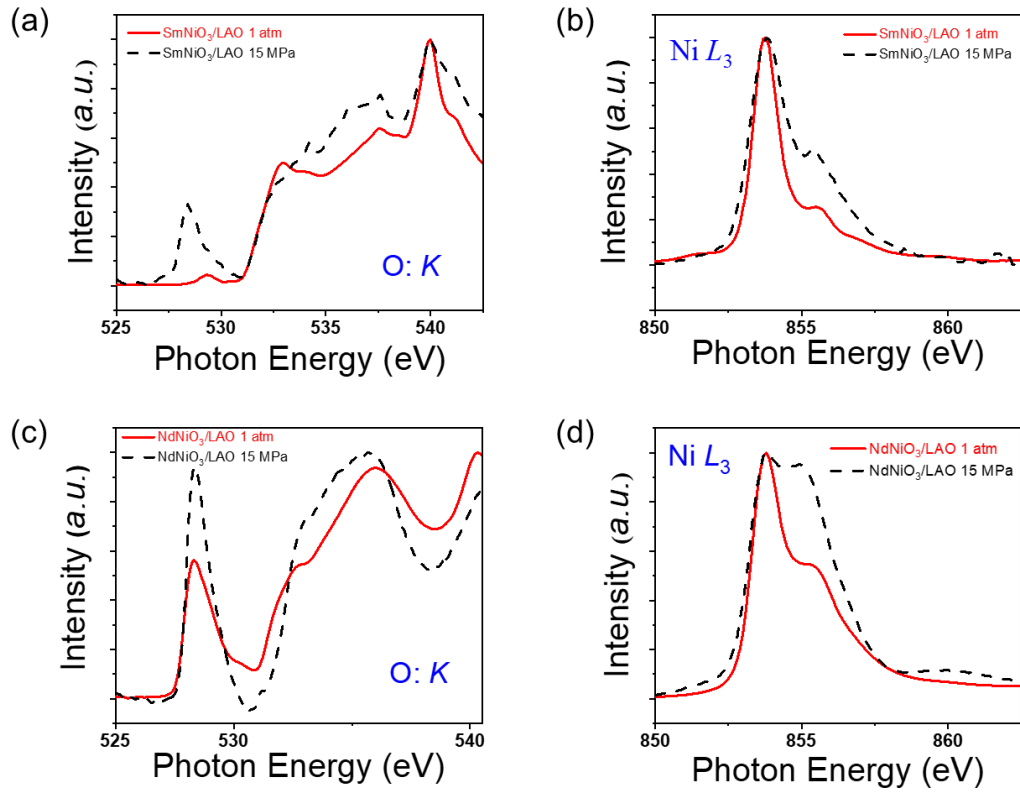


Fig. 4. Near edge X-ray absorption fine structure (NEXAFS) analysis of (a) O-K edge and (b) Ni- L_3 edge of SNO/LAO and (c) O-K edge and (d) Ni- L_3 edge of NNO/LAO with normal pressure and 15MPa. The data for SNO/LAO and NNO/LAO under 15MPa are from the reference ⁴⁴.

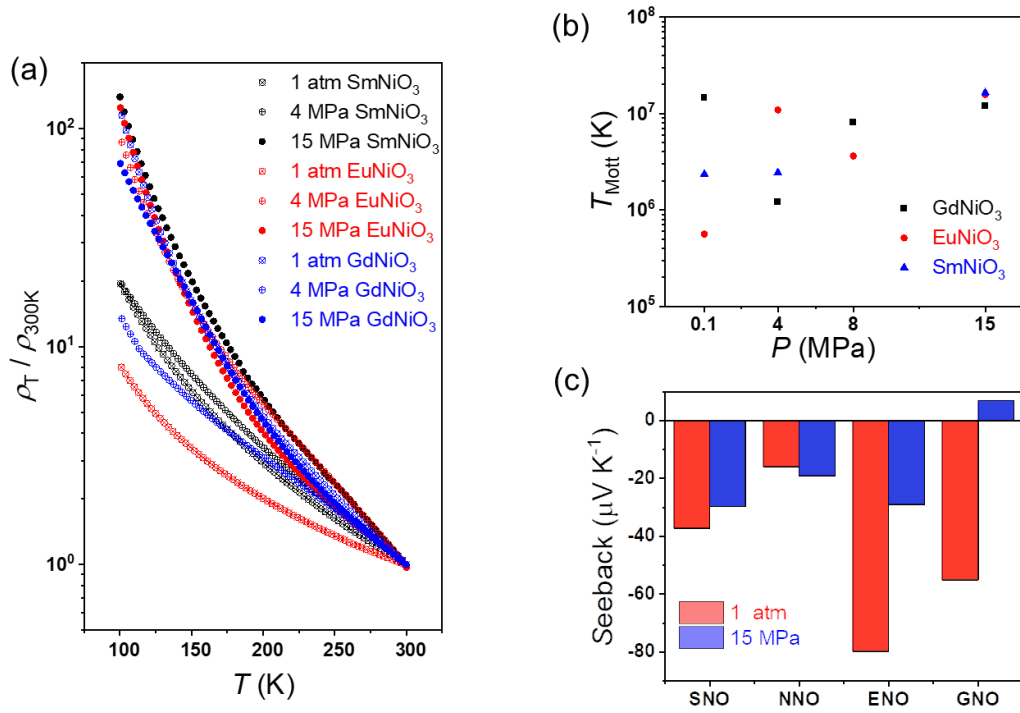


Fig. 5. (a) Illustration of ρ_T/ρ_{300K} versus Temperature for SNO, ENO and GNO grown on LAO under various oxygen pressure. And the data for GNO under 15MPa are from the reference ⁵³ (b) Oxygen pressure dependence of T_{Mott} for SNO, ENO and GNO deposited on LAO. (c) Seebeck coefficients at room temperature under 1atm and 15MPa for SNO, NNO, ENO and GNO grown on LAO.

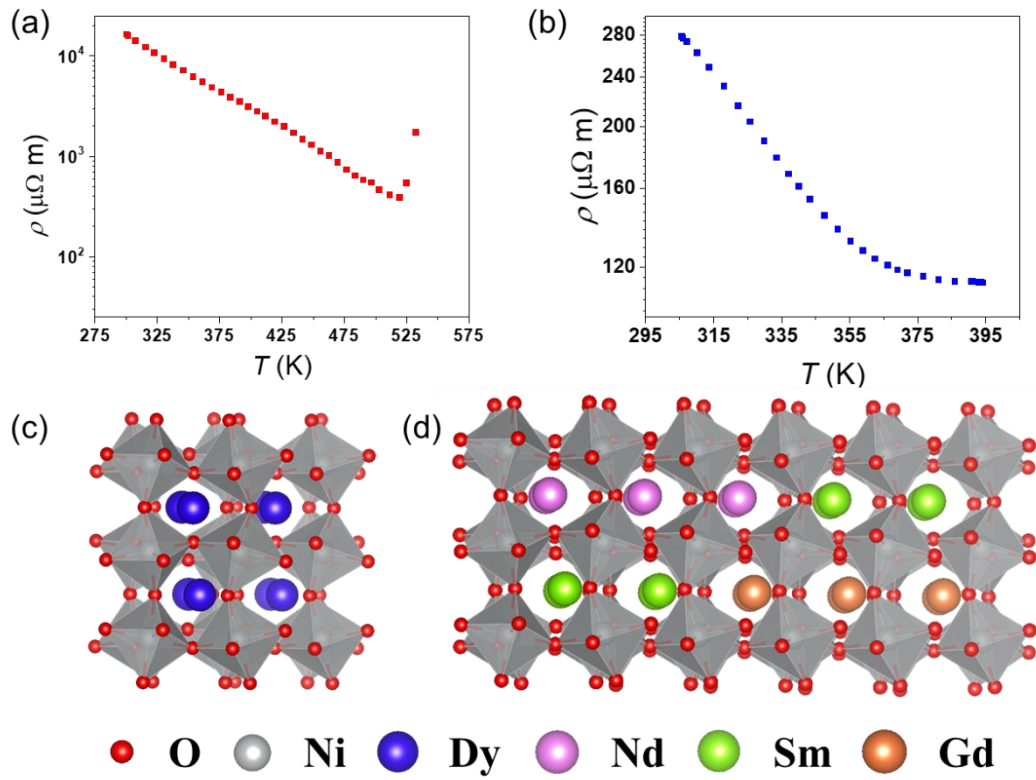


Fig. 6. Temperature dependence of the resistivity for (a) $\text{DyNiO}_3/\text{LaAlO}_3$ (001) and (b) $\text{Nd}_{0.3}\text{Sm}_{0.4}\text{Gd}_{0.3}\text{NiO}_3/\text{LaAlO}_3$ (001) under 15MPa. Schematic illustrations of the crystal structure for (c) DyNiO_3 and (d) $\text{Nd}_{0.3}\text{Sm}_{0.4}\text{Gd}_{0.3}\text{NiO}_3$, respectively.

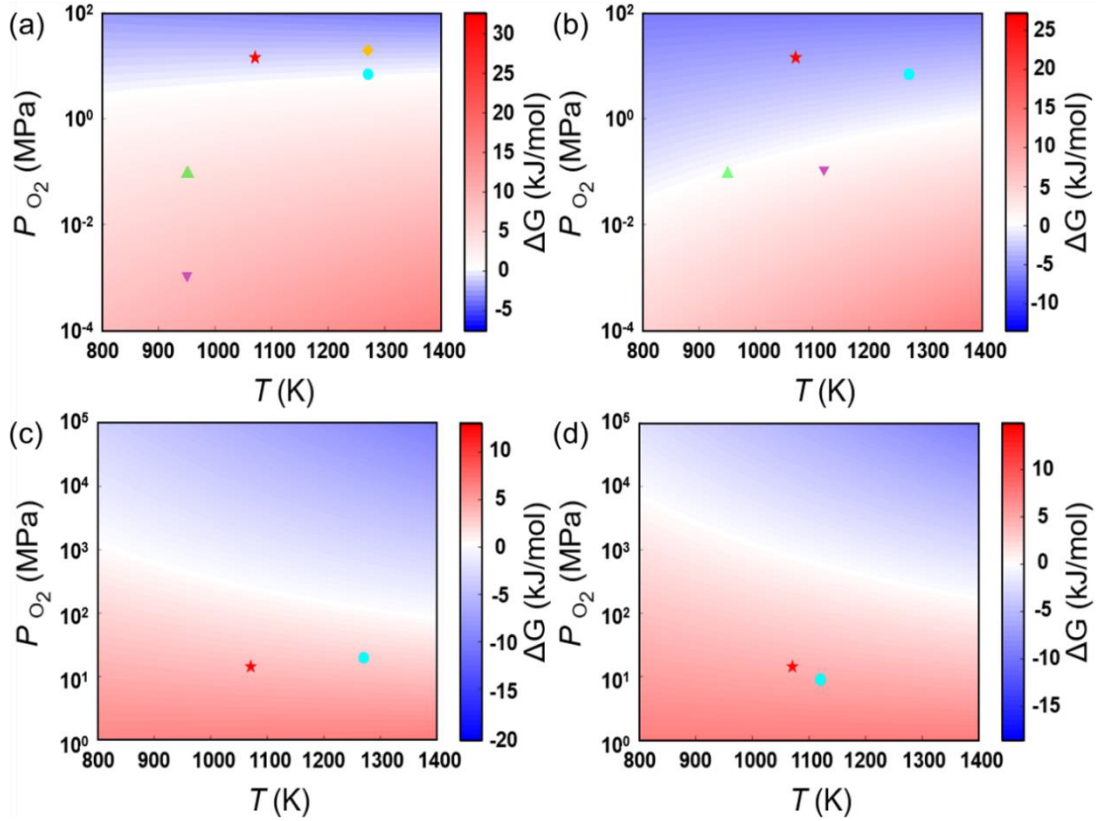


Fig. 7. Thermodynamic phase stability diagram for (a) SmNiO_3 , Solid red star (1073K 15MPa) indicates conditions leading to SNO/LAO (001) epitaxial films in this work. Solid cyan circle (1273K 7MPa) and solid orange diamond (1273K 20MPa) indicate synthesis conditions of SmNiO_3 powder reported in the reference ² and reference ⁶², respectively. Solid green upper triangular (953K 0.1MPa) and solid purple lower triangular (953K, 0.001MPa) indicate conditions of SmNiO_3 epitaxial films reported in the reference ³⁴ and reference ⁶³, respectively. (b) NdNiO_3 , Solid red star (1073K 15MPa) indicates conditions leading to NNO/LAO (001) epitaxial films in this work. Solid cyan circle (1273K 7MPa) indicates conditions of NdNiO_3 powder reported in the reference ². Solid green upper triangular (953K 0.1MPa) and solid purple lower triangular (1123K 0.1MPa) suggest conditions of NNO/LAO (001) and NNO/LAO (110) epitaxial films reported in the reference ³⁴ and reference ⁶⁴, respectively. (c) EuNiO_3 , Solid red star (1073K 15MPa) indicates conditions leading to ENO/LAO (001) epitaxial films in this work. Solid cyan circle (1273K 20MPa) represents condition for EuNiO_3 powder in the reference ⁶⁵. (d) GdNiO_3 , Solid red star (1073K 15MPa) indicates conditions leading to GNO/LAO (001) epitaxial films in this work. Solid cyan circle (1123K 9MPa) indicates conditions leading to powder GdNiO_3 ⁵⁵.

References

- 1 G. Catalan, *Phase Transit.*, 2008, **81**, 729-749.
- 2 M. T. Escote, A. M. L. da Silva, J. R. Matos and R. F. Jardim, *J. Solid State Chem.*, 2000, **151**, 298-307.
- 3 N. Shukla, T. Joshi, S. Dasgupta, P. Borisov, D. Lederman and S. Datta, *Appl. Phys. Lett.*, 2014, **105**, 012108.
- 4 J. Shi, S. D. Ha, Y. Zhou, F. Schoofs and S. Ramanathan, *Nat. Commun.*, 2013, **4**, 2676.
- 5 R. Scherwitzl, P. Zubko, I. G. Lezama, S. Ono, A. F. Morpurgo, G. Catalan and J. M. Triscone, *Adv. Mater.*, 2010, **22**, 5517-5520.
- 6 F. Conchon, A. Boulle, R. Guinebrière, C. Girardot, S. Pignard, J. Kreisel, F. Weiss, E. Dooryhée and J.-L. Hodeau, *Appl. Phys. Lett.*, 2007, **91**, 192110.
- 7 J. Chen, H. Hu, J. Wang, T. Yajima, B. Ge, X. Ke, H. Dong, Y. Jiang and N. Chen, *Mater. Horiz.*, 2019, **6**, 788-795.
- 8 F. Y. Bruno, K. Z. Rushchanskii, S. Valencia, Y. Dumont, C. Carrétéro, E. Jacquet, R. Abrudan, S. Blügel, M. Ležaić, M. Bibes and A. Barthélémy, *Phys. Rev. B*, 2013, **88**, 195108.
- 9 J. Shi, Y. Zhou and S. Ramanathan, *Nat. Commun.*, 2014, **5**, 4860.
- 10 J. Chen, W. Mao, B. Ge, J. Wang, X. Ke, V. Wang, Y. Wang, M. Döbeli, W. Geng, H. Matsuzaki, J. Shi and Y. Jiang, *Nat. Commun.*, 2019, **10**, 694.
- 11 Y. Zhou, S. Middey, J. Jiang, N. Chen, L. Chen, X. Shi, M. Döbeli, J. Shi, J. Chakhalian and S. Ramanathan, *Appl. Phys. Lett.*, 2015, **107**, 031905.
- 12 Y. Zhou, X. Guan, H. Zhou, K. Ramadoss, S. Adam, H. Liu, S. Lee, J. Shi, M. Tsuchiya, D. D. Fong and S. Ramanathan, *Nature*, 2016, **534**, 231-240.
- 13 Z. Zhang, D. Schwanz, B. Narayanan, M. Kotiuga, J. A. Dura, M. Cherukara, H. Zhou, J. W. Freeland, J. Li, R. Sutarto, F. He, C. Wu, J. Zhu, Y. Sun, K. Ramadoss, S. S. Nonnenmann, N. Yu, R. Comin, K. M. Rabe, S. Sankaranarayanan and S. Ramanathan, *Nature*, 2018, **553**, 68-72.
- 14 F. Zuo, P. Panda, M. Kotiuga, J. Li, M. Kang, C. Mazzoli, H. Zhou, A. Barbour, S. Wilkins, B. Narayanan, M. Cherukara, Z. Zhang, S. Sankaranarayanan, R. Comin, K. M. Rabe, K. Roy and S. Ramanathan, *Nat. Commun.*, 2017, **8**, 240.
- 15 J. Advanced Electronic Materials Chen, Z. Li, H. Dong, J. Xu, V. Wang, Z. Feng, Z. Chen, B. Chen, N. Chen and H. K. Mao, *Adv. Funct. Mater.*, 2020, **30**, 2000987.
- 16 C. Chen, J. Zhou, J. Geng, R. Bao, Z. Wang, J. Xia and H. Li, *Appl. Surf. Sci.*, 2020, **503**, 144287.
- 17 H. T. Zhang, F. Zuo, F. Li, H. Chan, Q. Wu, Z. Zhang, B. Narayanan, K. Ramadoss, I. Chakraborty, G. Saha, G. Kamath, K. Roy, H. Zhou, A. A. Chubykin, S. Sankaranarayanan, J. H. Choi and S. Ramanathan, *Nat. Commun.*, 2019, **10**, 1651.
- 18 R. Jaramillo, F. Schoofs, S. D. Ha and S. Ramanathan, *J. Mater. Chem. C*, 2013, **1**, 2455-2462.
- 19 R. Jaramillo, S. D. Ha, D. M. Silevitch and S. Ramanathan, *Nat. Phys.*, 2014, **10**, 304-307.
- 20 S. D. Ha, M. Otaki, R. Jaramillo, A. Podpirka and S. Ramanathan, *J. Solid State Chem.*, 2012, **190**, 233-237.
- 21 A. Ambrosini and J.-F. Hamet, *Appl. Phys. Lett.*, 2003, **82**, 727-729.
- 22 L. Chang, L. Wang, L. You, Z. Yang, A. Abdelsamie, Q. Zhang, Y. Zhou, L. Gu, S. A. Chambers and J. Wang, *ACS Appl. Mater. Interfaces*, 2019, **11**, 16191-16197.
- 23 M. A. Novojilov, O. Y. Gorbenko, I. E. Graboy, A. R. Kaul, H. W. Zandbergen, N. A. Babushkina and L. M. Belova, *Appl. Phys. Lett.*, 2000, **76**, 2041-2043.
- 24 G. Kresse and J. Furthmüller, *Phys. Rev. B*, 1996, **54**, 11169-11186.

- 25 P. E. Blöchl, *Phys. Rev. B*, 1994, **50**, 17953-17979.
- 26 J. P. Perdew, K. Burke and M. Ernzerhof, *Phys. Rev. Lett.*, 1996, **77**, 3865-3868.
- 27 S. Asanuma, P. H. Xiang, H. Yamada, H. Sato, I. H. Inoue, H. Akoh, A. Sawa, K. Ueno, H. Shimotani, H. Yuan, M. Kawasaki and Y. Iwasa, *Appl. Phys. Lett.*, 2010, **97**, 142110.
- 28 E. Sakai, K. Yoshimatsu, M. Tamamitsu, K. Horiba, A. Fujimori, M. Oshima and H. Kumigashira, *Appl. Phys. Lett.*, 2014, **104**, 171609.
- 29 L. Wang, Q. Zhang, L. Chang, L. You, X. He, K. Jin, L. Gu, H. Guo, C. Ge, Y. Feng and J. Wang, *Adv. Electron. Mater.*, 2017, **3**, 1700321.
- 30 A. Seifert, A. Vojta, J. S. Speck and F. F. Lange, *J. Mater. Res.*, 1996, **11**, 1470-1482.
- 31 Y. L. Zhu, S. J. Zheng, D. Chen and X. L. Ma, *Thin Solid Films*, 2010, **518**, 3669-3673.
- 32 J. Chen, H. Li, J. Wang, X. Ke, B. Ge, J. Chen, H. Dong, Y. Jiang and N. Chen, *J. Mater. Chem. A*, 2020, **8**, 13630-13637.
- 33 J. Chen, H. Hu, T. Yajima, J. Wang, B. Ge, H. Dong, Y. Jiang and N. Chen, *J. Mater. Chem. C*, 2019, **7**, 8101-8108.
- 34 M. A. Novojilov, O. Y. Gorbenko, I. V. Nikulin, I. E. Graboy, A. R. Kaul, N. A. Babushkina and L. M. Belova, *Int. J. Inorg. Mater.*, 2001, **3**, 1165-1168.
- 35 A. R. Kaul, O. Y. Gorbenko, I. E. Graboy, S. V. Samoilenkov, M. A. Novojilov, A. A. Bosak, H. W. Zandbergen and G. Wahl, *Int. J. Inorg. Mater.*, 2001, **3**, 1177-1180.
- 36 M. Kotiuga, Z. Zhang, J. Li, F. Rodolakis, H. Zhou, R. Sutarto, F. He, Q. Wang, Y. Sun, Y. Wang, N. A. Aghamiri, S. B. Hancock, L. P. Rokhinson, D. P. Landau, Y. Abate, J. W. Freeland, R. Comin, S. Ramanathan and K. M. Rabe, *Proc. Natl. Acad. Sci. U. S. A.*, 2019, **116**, 21992-21997.
- 37 U. Sidik, A. N. Hattori, R. Rakshit, S. Ramanathan and H. Tanaka, *ACS Appl. Mater. Interfaces*, 2020, **12**, 54955-54962.
- 38 W. Liang, H. Hou, Y. Lin and S.-N. Luo, *J. Phys. D: Appl. Phys.*, 2019, **52**, 075303.
- 39 H. Ji, G. Zhou, J. Zhang, X. Wang and X. Xu, *J. Rare Earths*, 2021, **39**, 317-322.
- 40 L. Wang, S. Dash, L. Chang, L. You, Y. Feng, X. He, K. J. Jin, Y. Zhou, H. G. Ong, P. Ren, S. Wang, L. Chen and J. Wang, *ACS Appl. Mater. Interfaces*, 2016, **8**, 9769-9776.
- 41 L. Wang, K. A. Stoerzinger, L. Chang, J. Zhao, Y. Li, C. S. Tang, X. Yin, M. E. Bowden, Z. Yang, H. Guo, L. You, R. Guo, J. Wang, K. Ibrahim, J. Chen, A. Rusydi, J. Wang, S. A. Chambers and Y. Du, *Adv. Funct. Mater.*, 2018, **28**, 1803712.
- 42 D. Yao, L. Shi, S. Zhou, H. Liu, Y. Wang, J. Zhao and Y. Li, *J. Phys. D: Appl. Phys.*, 2016, **49**, 125301.
- 43 P. H. Xiang, N. Zhong, C. G. Duan, X. D. Tang, Z. G. Hu, P. X. Yang, Z. Q. Zhu and J. H. Chu, *J. Appl. Phys.*, 2013, **114**, 243713.
- 44 J. Chen, H. Hu, J. Wang, C. Liu, X. Liu, Z. Li and N. Chen, *ACS Appl. Mater. Interfaces*, 2019, **11**, 34128-34134.
- 45 J. Chen, H. Hu, F. Meng, T. Yajima, L. Yang, B. Ge, X. Ke, J. Wang, Y. Jiang and N. Chen, *Matter*, 2020, **2**, 1296-1306.
- 46 B. Torriass, J. Margot and M. Chaker, *MRS Communications*, 2018, **8**, 183-188.
- 47 L. Zhang, H. J. Gardner, X. G. Chen, V. R. Singh and X. Hong, *J. Phys.: Condens. Matter*, 2015, **27**, 132201.
- 48 K. Ramadoss, N. Mandal, X. Dai, Z. Wan, Y. Zhou, L. Rokhinson, Y. P. Chen, J. Hu and S. Ramanathan, *Phys. Rev. B*, 2016, **94**, 235124.
- 49 M. Gregg, *Phys. Rev. B*, 2000, **62**, 7892-7900.

- 50 N. F. Mott, *Contemp. Phys.*, 1969, **10**, 125-138.
- 51 N. F. Mott, *Philos. Mag.*, 1969, **19**, 835-852.
- 52 S. D. Ha, R. Jaramillo, D. M. Silevitch, F. Schoofs, K. Kerman, J. D. Baniecki and S. Ramanathan, *Phys. Rev. B*, 2013, **87**.
- 53 J. Chen, F. Yan, H. Hu, J. Wang, Y. Jiang, N. Chen and J. Chen, *Appl. Phys. Lett.*, 2020, **116**, 051902.
- 54 J. L. García-Muñoz, R. Mortimer, A. Llobet, J. A. Alonso, M. J. Martínez-Lope and S. P. Cottrell, *Physica B*, 2006, **374-375**, 87-90.
- 55 J. A. Alonso, M. J. Martínez-Lope, M. T. Casais, J. L. Martínez, G. Demazeau, A. Largeau, J. L. García-Muñoz, A. Muñoz and M. T. Fernández-Díaz, *Chem. Mater.*, 1999, **11**, 2463-2469.
- 56 J. A. Alonso, M. J. Martínez-Lope, G. Demazeau, M. T. Fernández-Díaz, I. A. Presniakov, V. S. Rusakov, T. V. Gubaidulina and A. V. Sobolev, *Dalton Trans.*, 2008, DOI: 10.1039/B808485H, 6584-6592.
- 57 R. K. Patel, S. K. Ojha, S. Kumar, A. Saha, P. Mandal, J. W. Freeland and S. Middey, *Appl. Phys. Lett.*, 2020, **116**, 071601.
- 58 J. H. Park, J. M. Coy, T. S. Kasirga, C. Huang, Z. Fei, S. Hunter and D. H. Cobden, *Nature*, 2013, **500**, 431-434.
- 59 J. Cheng, A. Navrotsky, X.-D. Zhou and H. U. Anderson, *J. Mater. Res.*, 2011, **20**, 191-200.
- 60 R. Shannon, *Acta Crystallogr., Sect. A: Cryst. Phys., Diffr., Theor. Gen. Crystallogr.*, 1976, **32**, 751-767.
- 61 J. Chen, J. Chen, Z. Ren, D. Zhao, M. Wang, J. Miao, X. Xu, Y. Jiang and N. Chen, *J. Rare Earths*, 2021, **39**, 174-179.
- 62 N. E. Massa, A. Y. Ramos, H. C. N. Tolentino, N. M. Sousa-Neto, J. Fonseca and J. A. Alonso, *Mater. Res. Express*, 2015, **2**, 126301.
- 63 N. Ihzaz, S. Pignard, J. Kreisel, H. Vincent, J. Marcus, J. Dhahri and M. Oumezzine, *Phys. Status Solidi C*, 2004, **1**, 1679-1682.
- 64 X. Zhu, X. Tang, B. Wang, Y. Fu, J. Dai, W. Song, Z. Yang, X. Zhu, L. Chen and Y. Sun, *Cryst. Growth Des.*, 2010, **10**, 4682-4685.
- 65 H. Kobayashi, S. Ikeda, Y. Yoda, N. Hirao, Y. Ohishi, J. A. Alonso, M. J. Martínez-Lope, R. Lengsdorf, D. I. Khomskii and M. M. Abd-Elmeguid, *Phys. Rev. B*, 2015, **91**.

**Revealing the role of interfacial heterogeneous nucleation in metastable thin film
growth of rare-earth nickelates electronic transition materials**

Fengbo Yan^{1†}, Zhishan Mi^{1,2†}, Jinhao Chen¹, Haiyang Hu¹, Lei Gao^{1,3}, Jiaou Wang^{4*}, Nuofu*

Chen⁵, Yong Jiang¹, Lijie Qiao^{1,3} and Jikun Chen^{1}*

¹Beijing Advanced Innovation Center for Materials Genome Engineering, School of Materials Science and Engineering, University of Science and Technology Beijing, Beijing 100083, China

²China Iron & Steel Research Institute Group, Material Digital R&D Center, Beijing 100081, China

³Corrosion and Protection Center, University of Science and Technology Beijing, Beijing 100083, China

⁴Beijing Synchrotron Radiation Facility, Institute of High Energy Physics, Chinese Academy of Sciences, Beijing 100049, China

⁵School of Renewable Energy, North China Electric Power University, Beijing 102206, China

Correspondence: Prof. Lei Gao (gaolei@ustb.edu.cn), Prof. Jiaou Wang (wangjo@ihep.ac.cn), and Prof. Jikun Chen (jikunchen@ustb.edu.cn).

[†]Fengbo Yan and Zhishan Mi contributed equally to this work.

Section 1: XRD patterns at a broader scanning range for SNO/LAO, NNO/LAO, ENO/LAO and GNO/LAO

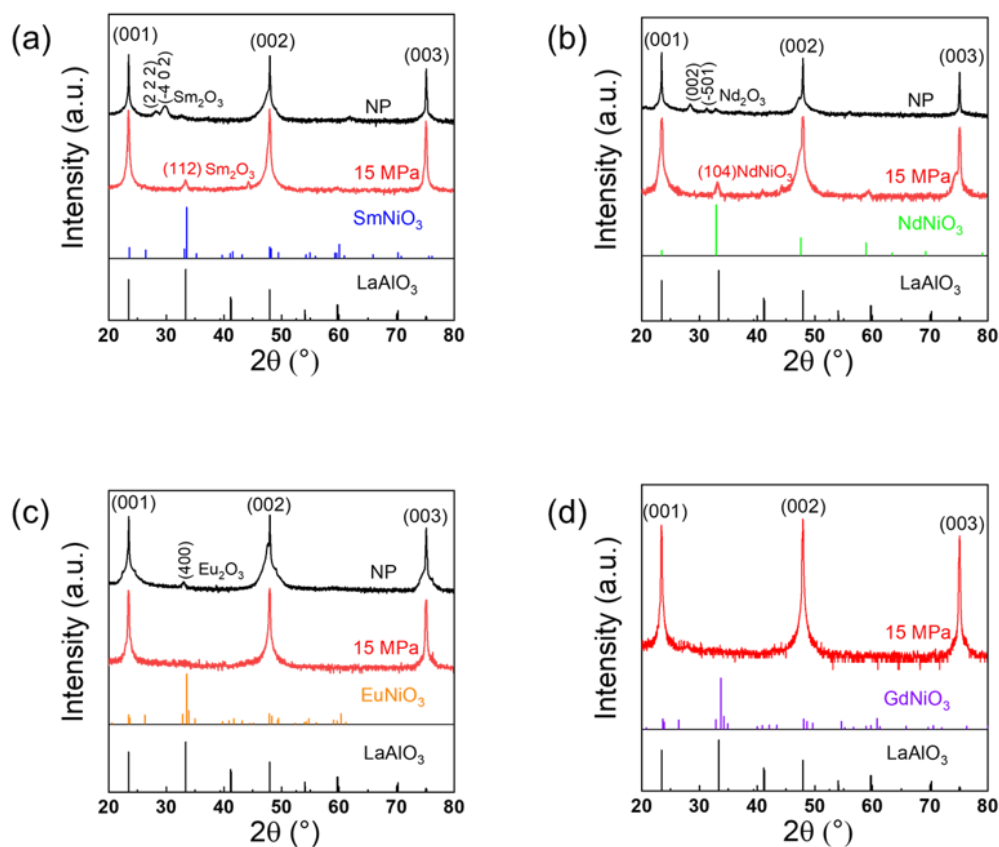


Fig. S1. X-ray diffraction patterns (θ - 2θ scans) of as-grown (a) $\text{SmNiO}_3/\text{LaAlO}_3(001)$ (b) $\text{NdNiO}_3/\text{LaAlO}_3(001)$ (c) $\text{EuNiO}_3/\text{LaAlO}_3(001)$ and (d) $\text{GdNiO}_3/\text{LaAlO}_3(001)$ thin films from 20° - 80° under various annealing oxygen pressures.

Section 2: Calculation of lattice strain of the a-axis and b-axis

LaAlO_3 has rhombohedral structure, which is defined as pseudo-cubic symmetry in order to finish the calculation. As for SrTiO_3 , it is cubic structure. Therefore, we adopted the LaAlO_3 and SrTiO_3 as cubic structure with relaxed lattice constants of $a_0=3.82 \text{ \AA}$ and $a_0=3.96 \text{ \AA}$, respectively. The orientation relationships between the rare-earth thin films and substrates follow $(001)_{\text{film}} // (001)_{\text{substrate}}$, $[100]_{\text{film}} // [110]_{\text{substrate}}$. According to this orientation relationship we built the interface supercells and set the reference lattice constants of interface structures as $b_0=5.40 \text{ \AA}$ (LaAlO_3 interface) and $b_0=5.60 \text{ \AA}$ (SrTiO_3 interface), respectively. The optimized lattice constants of rare-earth nickelates are listed in the following Table S1. And we calculated the lattice strain of a-axis and b-axis between rare-earth thin films and substrates using $\varepsilon_a=(a-b_0)/b_0$, $\varepsilon_b=(b-b_0)/b_0$. The obtained results are in the manuscript Table 1.

Table S1

The optimized lattice constants of rare-earth nickelates in a-axis and b-axis (unit: Å)

	a	b
SmNiO ₃	5.28753	5.44663
NdNiO ₃	5.32534	5.46882
EuNiO ₃	5.33896	5.35262
GdNiO ₃	5.24442	5.51225

Section 3: Interfacial charge transfer for *R*eNiO₃ grown on LAO(001) and STO(001) substrates

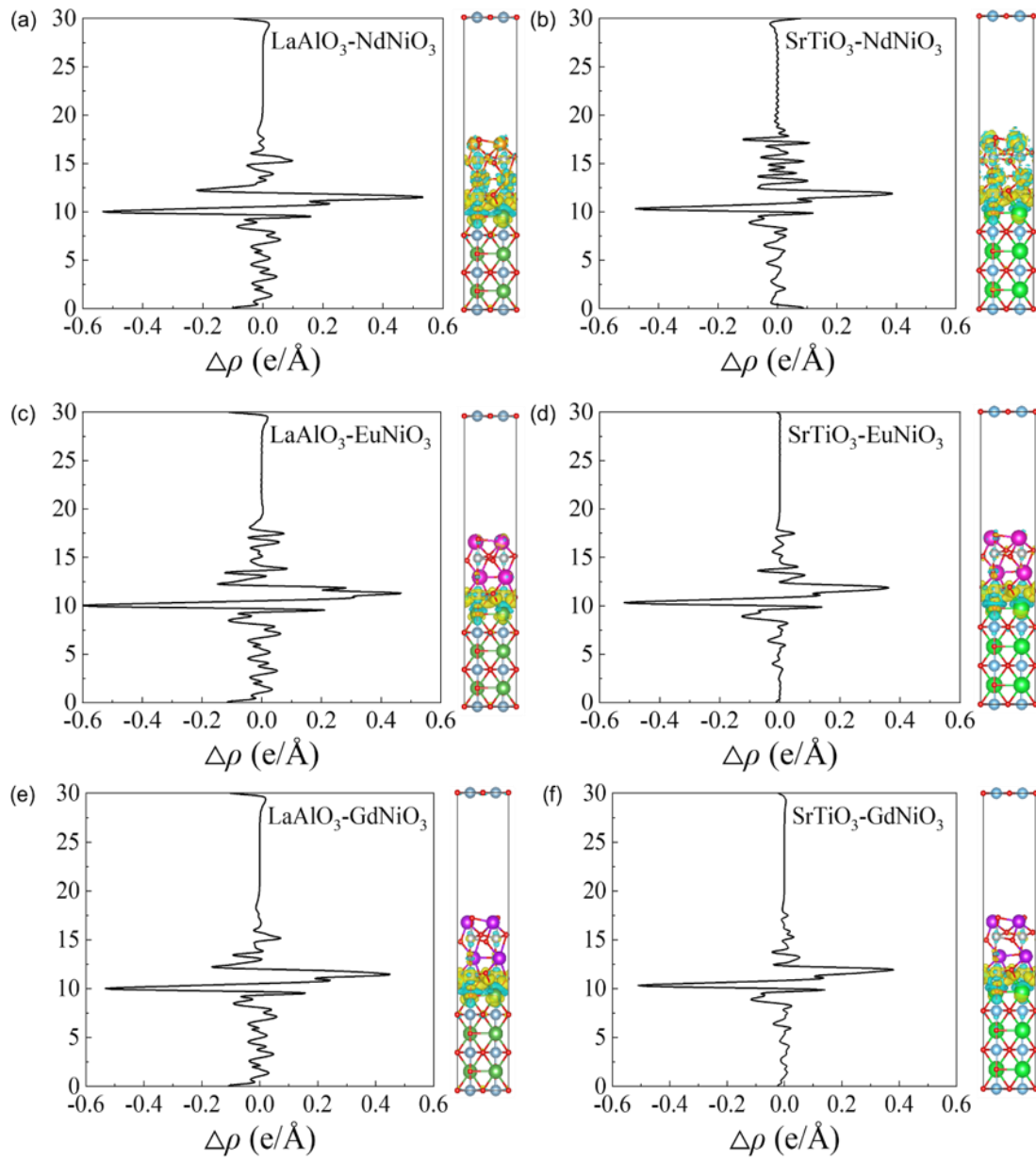


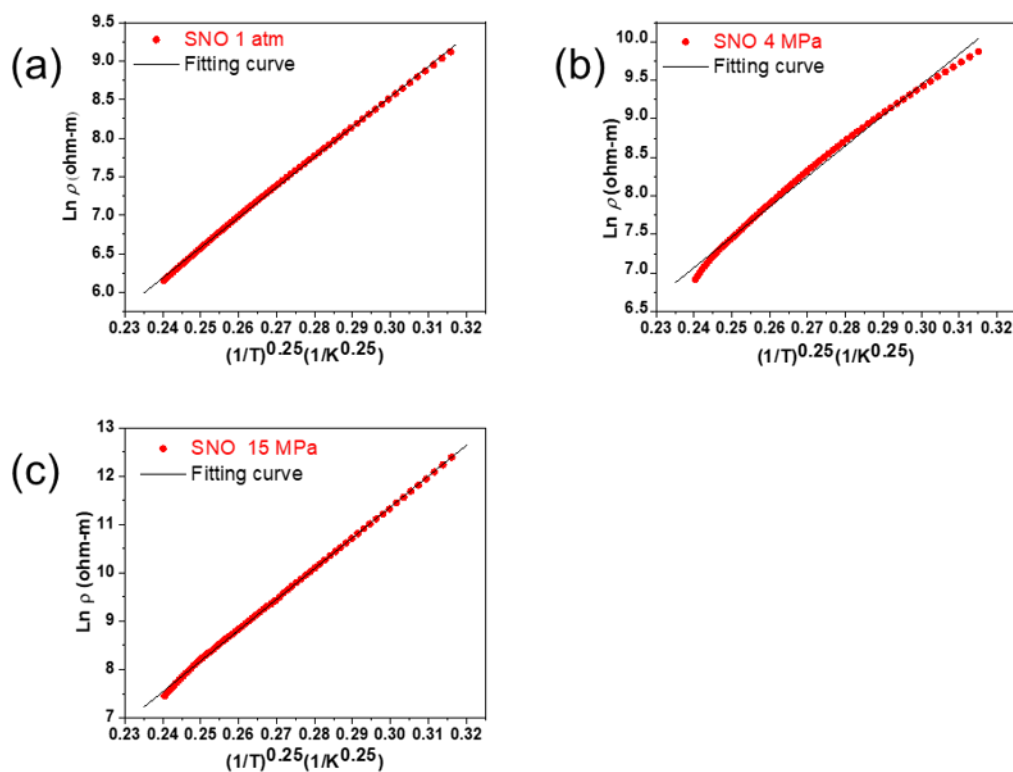
Fig. S2. The interfacial charge transfer of (a) LaAlO₃-NdNiO₃ interface (b) SrTiO₃-NdNiO₃ interface (c) LaAlO₃-EuNiO₃ interface (d) SrTiO₃-EuNiO₃ interface (e) LaAlO₃-GdNiO₃ interface (f) SrTiO₃-GdNiO₃ interface.

Section 4: Details about Mott variable range hopping model fitting low temperature R - T curves of rare-earth nickelates

In this part, the process of how to use the Mott variable range hopping (VRH) ¹ model to fit the low temperature R - T curves of rare-earth nickelates will be illustrated, from which we can obtain electrical parameters to describe the conduction mechanism at low temperature. The correlated formula ² is given by

$$\rho(T) = \rho_0 \exp \left(\frac{T_0}{T} \right)^p \quad (S1)$$

where ρ_0 is the prefactor, T_0 is the characteristic temperature which represents the degree of disorder in the film ³, and p is the exponent depending on the conduction mechanism which is related to the density of states (DOS) near Fermi energy (E_F). In the light of Mott ⁴, when the DOS is constant, $p=1/(1+D)$ where D is the dimensionality of the conduction system, indicating $p=1/4$ in three dimensions. Localized charge carriers near the Fermi level can hop from one localized state to another due to thermal fluctuation or an electrical field provided by external factors. Fig. S4 shows the plots of $\ln \rho(T)$ versus $T^{-0.25}$ from 100K to a certain temperature decided by two temperature values, metal-insulator transition temperature and 300K for $ReNiO_3$ ($Re=Sm, Eu, Gd$) thin films grown on $LaAlO_3$ (001) substrates annealing at various oxygen pressures.



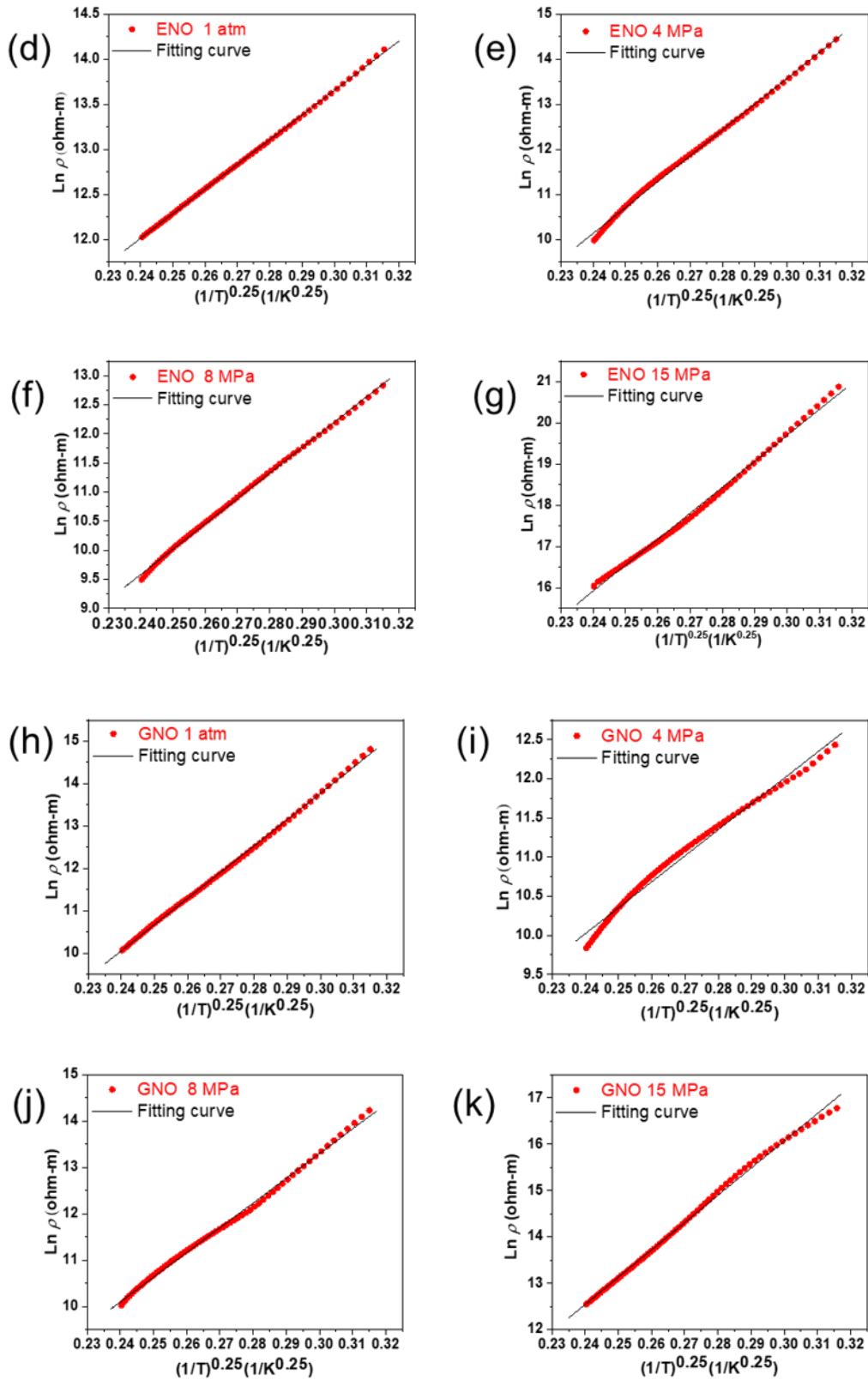


Fig. S3. Plots of $\text{Ln}(\rho_T) - T^{-0.25}$ for (a) SmNiO_3 0.1 MPa (b) SmNiO_3 4 MPa (c) SmNiO_3 15 MPa (d) EuNiO_3 0.1 MPa (e) EuNiO_3 4 MPa (f) EuNiO_3 8 MPa (g) EuNiO_3 15 MPa (h) GdNiO_3 0.1 MPa (i) GdNiO_3 4 MPa (j) GdNiO_3 8 MPa (k) GdNiO_3 15 MPa (data from reference ⁵) grown on $\text{LaAlO}_3(001)$ substrates. Black lines are the linear fitting curves.

According to eqn (S1), when $p=1/4$, the corresponding T_0 (T_{Mott}) for each condition can be obtained from the slope of the fitting curve in Fig. S4, which is listed in the Table S2. On the other hand, according to the reference ³, the localization length can be calculated by

$$T_0 \equiv T_{\text{Mott}} = \frac{18}{k_B N(E_F) a^3} \quad (\text{S2})$$

where $N(E_F)$ is the DOS near the E_F and a is the localization length. We take $N(E_F) = 1.5 \times 10^{18} \text{ eV}^{-1} \text{ cm}^{-3}$ ⁴. The calculation results of localization length a are also tabulated in the Table S2. The room temperature ($T=300 \text{ K}$) optimum average hopping energy (W_h) and hopping distance (R_h) for Mott-VRH model are estimated using the following expressions

$$R_h = \left(\frac{9a}{8\pi k_B T N(E_F)} \right)^{1/4} \quad (\text{S3})$$

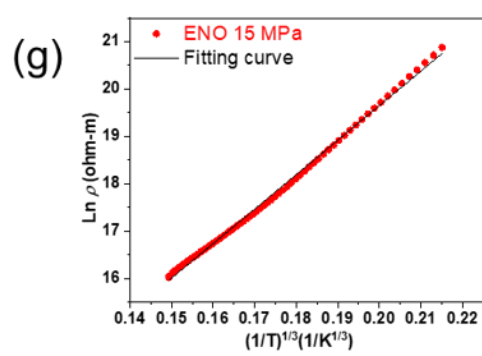
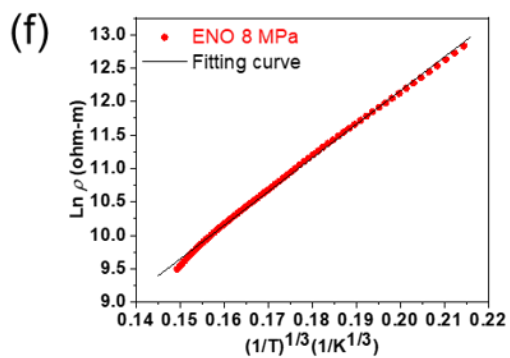
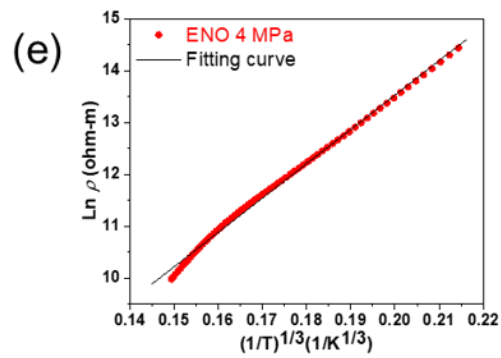
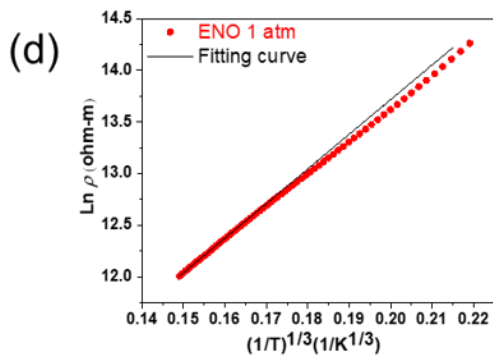
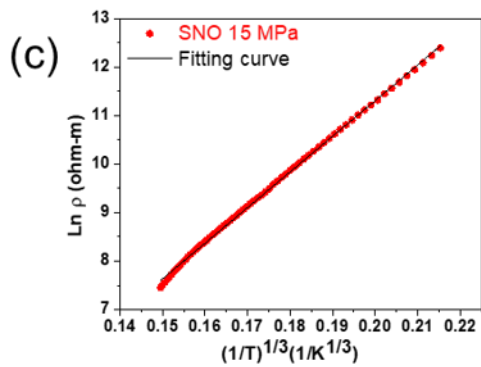
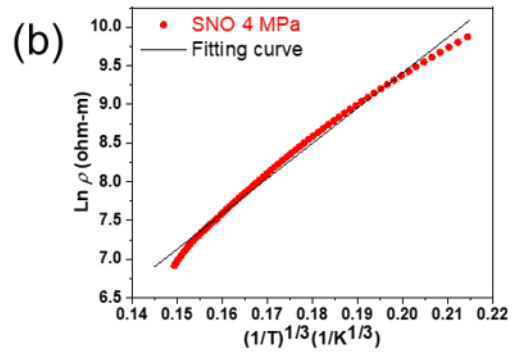
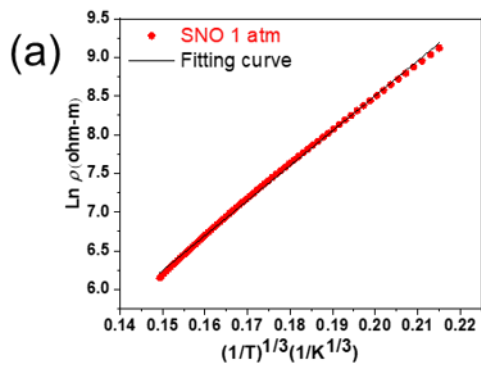
$$W_h = \frac{3}{4\pi R_h^3 N(E_F)} \quad (\text{S4})$$

In order to verify the validity of the fits for Mott VRH in ReNiO_3 thin films, it is necessary to calculate the values of R_h/a and $W_h/k_B T$ listed in the Table S2 as well. Obviously, the two criteria (1) $R_h/a > 1$ and (2) $W_h/k_B T > 1$ are satisfied, which proves the consistency of the fits. As shown in Table S2, T_{Mott} and localization length a are found to be different for various annealing oxygen pressures, which means the annealing oxygen pressure has an influence on the film formation process. The results show a trend with an increase in T_{Mott} as ρ of the film increases, which signifies films with high resistivity display a stronger localization behavior, which can be concluded from the Fig. S4 and Table S2. This trend has also been reported in other oxides ^{6, 7}.

Table S2

Parameters of Mott-VRH hopping mechanism in the ReNiO_3 ($\text{Re}=\text{Sm}, \text{Eu}, \text{Gd}$) thin films at various oxygen pressures.

Sample	$T_{\text{Mott}}(\text{K})$	$a(\text{nm})$	$T_{\text{max}}(\text{K})$	$R_{h\text{min}}(\text{nm})$	R_h/a	$W_h(\text{eV})$	$W_h/k_B T$
SNO 0.1 MPa	2.35E+06	3.90	300	13.77	3.53	0.0609	2.36
SNO 4 MPa	2.44E+06	3.85	300	13.73	3.57	0.0615	2.38
SNO 15 MPa	1.65E+07	2.04	300	11.71	5.75	0.0991	3.83
ENO 0.1 MPa	5.60E+05	6.29	300	15.52	2.47	0.0425	1.64
ENO 4 MPa	1.09E+07	2.34	300	12.12	5.19	0.0894	3.46
ENO 8 MPa	3.63E+06	3.37	300	13.28	3.94	0.0679	2.63
ENO 15 MPa	1.58E+07	2.07	300	11.75	5.69	0.0981	3.79
GNO 0.1 MPa	1.47E+07	2.12	300	11.82	5.59	0.0963	3.73
GNO 4 MPa	1.22E+06	4.85	300	14.55	3.00	0.0517	2.00
GNO 8 MPa	8.08E+06	2.58	300	12.43	4.81	0.0829	3.21
GNO 15 MPa	1.20E+07	2.26	300	12.02	5.31	0.0915	3.54



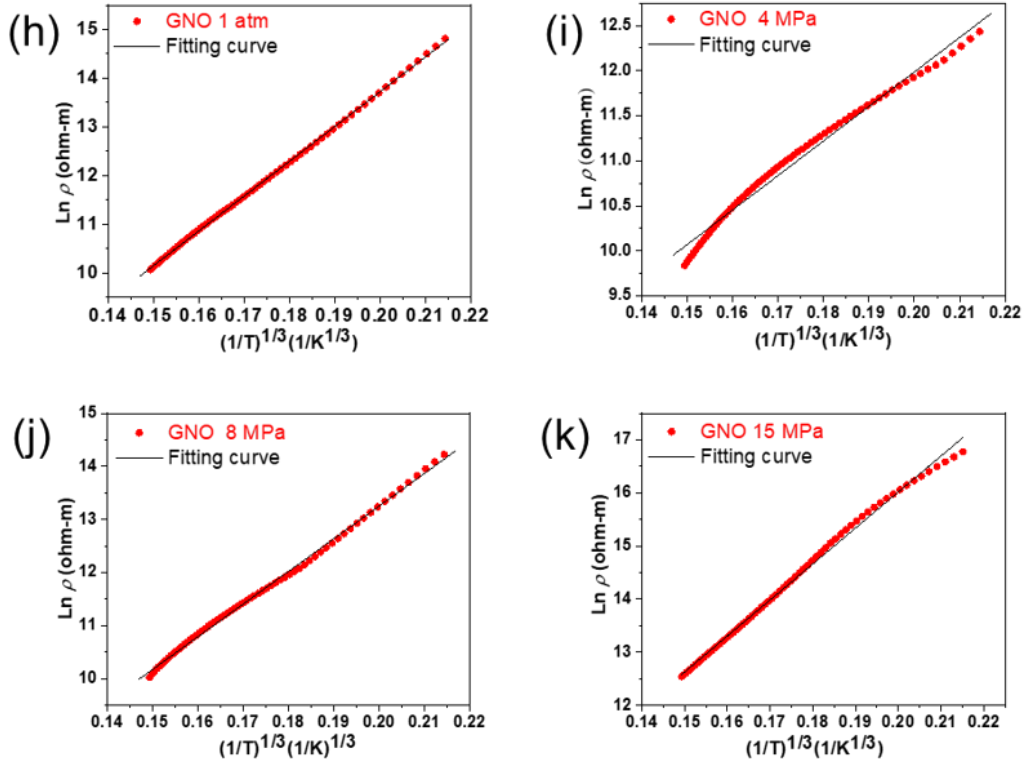


Fig. S4. Plots of $\ln(\rho_T)-T^{-1/3}$ for (a) SmNiO_3 0.1 MPa (b) SmNiO_3 4 MPa (c) SmNiO_3 15 MPa (d) EuNiO_3 0.1 MPa (e) EuNiO_3 4 MPa (f) EuNiO_3 8 MPa (g) EuNiO_3 15 MPa (h) GdNiO_3 0.1 MPa (i) GdNiO_3 4 MPa (j) GdNiO_3 8 MPa (k) GdNiO_3 15 MPa (data from reference ⁵) grown on $\text{LaAlO}_3(001)$ substrates. Black lines are the linear fitting curves.

Considering the thickness of as-grown ReNiO_3 thin films (about 10 nm), we also fit the $\ln(\rho_T)-T$ tendencies via two-dimensional carrier transport model. For the situation of two dimensions, $p=1/3$. Using similar method, the fitting plots of $\ln(\rho_T)-T^{-1/3}$ for various ReNiO_3 can be obtained in Fig. S5. According to the reference ³, the localization can be obtained by

$$T_0 \equiv T_{Mott} = \frac{13}{k_B N(E_F) a^2} \quad (\text{S5})$$

where $N(E_F)$ is the DOS near the E_F and a is the localization length. The calculation results are listed in Table S3.

In order to verify the correctness of the fits with the Mott VRH for ReNiO_3 , we calculate the hopping distance R_h by formula (S6) and the average hopping energy W_h by formula (S7) to confirm whether the two conditions $R_h/a > 1$ and $W_h/(k_B T) > 1$ are satisfied. The results are listed in the table S3 as well.

$$R_h = \left(\frac{9a}{8\pi k_B T N(E_F)} \right)^{1/3} \quad (\text{S6})$$

$$W_h = \frac{3}{4\pi R_h^2 N(E_F)} \quad (\text{S7})$$

Table S3

Parameters of Mott-VRH hopping mechanism in the $ReNiO_3$ ($Re=Sm, Eu, Gd$) thin films at various oxygen pressure.

Sample	$T_{Mott}(K)$	$a(nm)$	$T_{max}(K)$	$R_{hmin}(nm)$	R_h/a	$W_h(eV)$	$W_h/k_B T$
SNO 0.1 MPa	9.21E+04	0.010	300	0.021	2.04	0.0351	1.36
SNO 4 MPa	9.46E+04	0.010	300	0.021	2.06	0.0355	1.37
SNO 15 MPa	3.97E+05	0.005	300	0.017	3.32	0.0572	2.21
ENO 0.1 MPa	3.77E+04	0.016	300	0.025	1.51	0.0261	1.01
ENO 4 MPa	2.91E+05	0.006	300	0.018	2.99	0.0515	1.99
ENO 8 MPa	1.28E+05	0.009	300	0.020	2.27	0.0392	1.52
ENO 15 MPa	3.86E+05	0.005	300	0.017	3.28	0.0567	2.19
GNO 0.1 MPa	3.66E+05	0.013	300	0.017	3.22	0.0556	2.15
GNO 4 MPa	5.62E+04	0.007	300	0.023	1.72	0.0298	1.15
GNO 8 MPa	2.33E+05	0.006	300	0.018	2.78	0.0479	1.85
GNO 15 MPa	3.12E+05	2.26	300	0.017	3.06	0.0528	2.14

We can notice that similar results are in two dimensions as in three dimensions, which shows the two dimensions Mott VRH model is also satisfied generally.

Section 5: Estimation of parameters of h and s in molar Gibbs free energy of formation of bulk $ReNiO_3$

According to the reference ⁸, the molar Gibbs free energy of formation of bulk $ReNiO_3$ can be estimated from the following:

$$\Delta G = \Delta H_{LNO,1000K} - T\Delta S_{LNO,1000K} + (h - sT)(r(Re^{3+}) - r(La^{3+})) - (1/4)RT\ln(P/p) \quad (S8)$$

where LNO stands for $LaNiO_3$, T is the absolute temperature, R is the ideal gas constant, the P represents oxygen pressure with MPa unit, p represents the standard atmospheric pressure (0.1 MPa) and $r(Re^{3+})$ and $r(La^{3+})$ are the radii of Re^{3+} and La^{3+} , respectively. According to the reference ⁹, the enthalpy and entropy changes for the formation of $LaNiO_3$ from oxides and O_2 at 1000K are $\Delta H_{LNO,1000K} = -46.07 \text{ kJmol}^{-1}$ and $\Delta S_{LNO,1000K} = -26.4 \times 10^{-3} \text{ kJK}^{-1}\text{mol}^{-1}$. h and s represent the trend in enthalpy and entropy with variation of ionic radii. They can be estimated from the following process. As mentioned in the reference ⁸, the value of h is calculated using a statistically weighted averaged of linear slope from ΔG vs. $r(Re^{3+})$ for $ReMnO_3$, $ReFeO_3$ and $ReCoO_3$, which has been obtained that $h = -207 \text{ kJmol}^{-1}\text{\AA}^{-1}$. As a typical rare-earth nickelate perovskite, the synthesis conditions of $SmNiO_3$ have been widely investigated. It is accepted that the molar Gibbs free energy of formation of bulk $SmNiO_3$ is zero at the lowest pressure for high temperature synthesis of $SmNiO_3$, and the lowest pressure for successful high temperature synthesis of $SmNiO_3$ is reported by Escote *et al.* (1273 K, 70 bar) ¹⁰. This condition was further used to estimate the value of s . On the other hand, the radii of rare-earth elements are obtained from the reference ¹¹. Based on these conditions, the value of s is estimated as $-0.00744 \text{ kJK}^{-1}\text{mol}^{-1}\text{\AA}^{-1}$. It is clear the value of s is much smaller than the value of h , indicating the assumption is effective.

References

- 1 L. Zhang, H. J. Gardner, X. G. Chen, V. R. Singh and X. Hong, *J. Phys.: Condens. Matter*, 2015, **27**, 132201.
- 2 N. F. Mott, *Philos. Mag.*, 1969, **19**, 835-852.
- 3 N. F. Mott and E. A. Davis, *Electronic processes in non-crystalline materials*, Oxford university press, 2012.
- 4 K. Ramadoss, N. Mandal, X. Dai, Z. Wan, Y. Zhou, L. Rokhinson, Y. P. Chen, J. Hu and S. Ramanathan, *Phys. Rev. B*, 2016, **94**, 235124.
- 5 J. Chen, F. Yan, H. Hu, J. Wang, Y. Jiang, N. Chen and J. Chen, *Appl. Phys. Lett.*, 2020, **116**, 051902.
- 6 V. V. Poltavets, M. Greenblatt, G. H. Fecher and C. Felser, *Phys. Rev. Lett.*, 2009, **102**, 046405.
- 7 M. Jenderka, J. Barzola-Quiquia, Z. Zhang, H. Frenzel, M. Grundmann and M. Lorenz, *Phys. Rev. B*, 2013, **88**, 045111
- 8 R. Jaramillo, F. Schoofs, S. D. Ha and S. Ramanathan, *J. Mater. Chem. C*, 2013, **1**, 2455-2462.
- 9 J. Cheng, A. Navrotsky, X.-D. Zhou and H. U. Anderson, *J. Mater. Res.*, 2011, **20**, 191-200.
- 10 M. T. Escote, A. M. L. da Silva, J. R. Matos and R. F. Jardim, *J. Solid State Chem.*, 2000, **151**, 298-307.
- 11 R. Shannon, *Acta Crystallogr., Sect. A: Cryst. Phys., Diffr., Theor. Gen. Crystallogr.*, 1976, **32**, 751-767.